

1 **Title**

2 EROS is a selective chaperone regulating the phagocyte NADPH oxidase and purinergic
3 signalling

4 **Authors**

5 Lyra O. Randzavola^{1*}, Paige M. Mortimer^{1*}, Emma Garside¹, Elizabeth R. Dufficy², Andrea
6 Schejtman³, Georgia Roumelioti⁴, Lu Yu⁴, Mercedes Pardo⁴, Kerstin Spirohn^{5,6,7}, Charlotte Tolley⁸,
7 Cordelia Brandt⁸, Katherine Harcourt⁸, Esme Nichols¹, Mike Nahorski⁹, Geoff Woods⁹, James C.
8 Williamson^{2,10}, Shreehari Suresh², John M. Sowerby^{2,10}, Misaki Matsumoto¹¹, Celio X.C. Santos¹²,
9 Cher Shen Kiar¹³, Subhankar Mukhopadhyay¹³, Will M. Rae^{2,10}, Gordon J. Dougan², John
10 Grainger¹⁴, Paul J. Lehner^{2,10}, Michael A. Calderwood^{5,6,7}, Jyoti Choudhary⁴, Simon Clare⁸,
11 Anneliese Speak⁸, Giorgia Santilli³, Alex Bateman¹⁵, Kenneth G. C. Smith^{2,10*}, Francesca
12 Magnani^{16*}, David C. Thomas^{*1}

13 **Affiliations:**

14 ¹ Department of Immunology and Inflammation, Centre for Inflammatory Disease, Imperial College
15 London, London, W12 0NN, United Kingdom

16 ² The Department of Medicine, University of Cambridge School of Clinical Medicine, Cambridge,
17 CB2 0SP, United Kingdom

18 ³ Molecular Immunology Unit, UCL Great Ormond Street Institute of Child Health, London, WC1N
19 1EH, United Kingdom

20 ⁴ Functional Proteomics, Division of Cancer Biology, Institute of Cancer Research, London, SW7
21 3RP, United Kingdom

22 ⁵ Center for Cancer Systems Biology (CCSB), Dana-Farber Cancer Institute, Boston, MA, USA

23 ⁶ Department of Genetics, Blavatnik Institute, Harvard Medical School, Boston, MA, 02215, USA

24 ⁷ Department of Cancer Biology, Dana-Farber Cancer Institute, Boston, MA, 02215, USA

25 ⁸ Wellcome Trust Sanger Institute, Hinxton, CB10 1RQ, United Kingdom

26 ⁹ Cambridge Institute of Medical Research, University of Cambridge, Cambridge, CB2 0XY, United
27 Kingdom

28 ¹⁰ Cambridge Institute of Therapeutic Immunology & Infectious Disease, Jeffrey Cheah Biomedical
29 Centre Cambridge Biomedical Campus, Cambridge, CB2 0AW, United Kingdom

30 ¹¹ Department of Pharmacology, Kyoto Prefectural University of Medicine, Kyoto 602-8566, Japan

31 ¹² School of Cardiovascular Medicine and Sciences, James Black Centre, King's College London,
32 London, SE5 9NU, United Kingdom

33 ¹³ Peter Gorer department of Immunobiology, School of Immunology & Microbial Sciences, King's
34 College London, London, SE1 9RT, United Kingdom

35 ¹⁴ Lydia Becker Institute of Immunology and Inflammation, Faculty of Biology, Medicine and
36 Health, University of Manchester, Manchester, M13 9PL, United Kingdom

37 ¹⁵ European Molecular Biology Laboratory, European Bioinformatics Institute, Wellcome Trust
38 Genome Campus, Hinxton, CB10 1SD, United Kingdom

39 ¹⁶ Department of Biology and Biotechnology, University of Pavia, Pavia, 27100, Italy

40 * These authors contributed equally to this work.

41 Corresponding authors: David C. Thomas. Email: david.thomas1@imperial.ac.uk, Francesca
42 Magnani: francesca.magnani@unipv.it

43 **Abstract**

44 EROS (Essential for Reactive Oxygen Species) protein is indispensable for expression of
45 gp91 phox , the catalytic core of the phagocyte NADPH oxidase. EROS deficiency in humans is a
46 novel cause of the severe immunodeficiency, chronic granulomatous disease (CGD), but its
47 mechanism of action was unknown until now. We elucidate the role of EROS, showing it acts at
48 the earliest stages of gp91 phox maturation. It binds the immature 58kDa gp91 phox directly,
49 preventing gp91 phox degradation and allowing glycosylation via the oligosaccharyltransferase
50 (OST) machinery and the incorporation of the heme prosthetic groups essential for catalysis.
51 EROS also regulates the purine receptors P2X7 and P2X1 through direct interactions and P2X7 is
52 almost absent in EROS deficient mouse and human primary cells. Accordingly, lack of murine
53 EROS results in markedly abnormal P2X7 signalling, inflammasome activation and T cell
54 responses. The loss of both ROS and P2X7 signalling leads to resistance to influenza infection in
55 mice. Our work identifies EROS as a highly selective chaperone for key proteins in innate and
56 adaptive immunity and a rheostat for immunity to infection. It has profound implications for our
57 understanding of immune physiology, ROS dysregulation and possibly gene therapy.

58 Introduction

59 The phagocyte nicotinamide adenine dinucleotide phosphate (NADPH oxidase) generates reactive
60 oxygen species (ROS) for host defence and is a critical component of innate immunity. This multi-
61 subunit protein complex consists of (i) a membrane bound heterodimer, gp91*phox*-p22*phox* and
62 (ii) the cytosolic components p67*phox* (Volpp et al., 1988, Nuno et al., 1988), p47*phox* (Volpp et
63 al., 1988, Segal et al., 1985), p40*phox* (Wientjes et al., 1993) and either Rac1 (Abo et al., 1991) or
64 Rac2 (Knaus et al., 1991). When activated by microbial stimuli, the complex facilitates the transfer
65 of electrons from cytosolic NADPH through the gp91*phox* (Nox2) protein to molecular oxygen,
66 located either extracellularly or within phagosomes (Segal, 2005, Thomas, 2017) generating
67 superoxide anions. Various chemical reactions then drive the production of further antimicrobial
68 ROS such as hydrogen peroxide (H₂O₂) and hypochlorous acid. Moreover, oxidation of key
69 cysteine residues driven by H₂O₂ has been implicated in regulating other immune pathways such
70 as inflammasome activation (Meissner et al., 2010), type 1 interferon production (Holmdahl et al.,
71 2016, Sareila et al., 2017, Olsson et al., 2017, Zhong et al., 2018), LC3-associated phagocytosis
72 (Martinez et al., 2015, Martinez et al., 2016) and autophagy (Thomas, 2018, de Luca et al., 2014).
73 The importance of the phagocyte NADPH oxidase is underlined by chronic granulomatous disease
74 (CGD), a severe monogenic immunodeficiency caused by loss of individual components, which
75 presents as susceptibility to infections with catalase positive organisms (including *Staphylococcus*
76 *Aureus*, *Salmonella* and *Burkholderia* species) but also with autoinflammatory manifestations,
77 characterised by sterile granulomatous inflammation (Alimchandani et al., 2013, Salvator et al.,
78 2015, Goldblatt et al., 1999). Conversely, excess ROS generation can be damaging to tissues via
79 e.g., lipid peroxidation and have been implicated in the pathogenesis of autoimmunity (Choi et al.,
80 2015, Hartung et al., 1988, Noubade et al., 2014). Polymorphisms in the genes encoding subunits
81 are also implicated in numerous autoimmune diseases (Magnani et al., 2014).

82 One way to control ROS generation is to regulate the abundance of gp91*phox*-p22*phox*, the
83 critical membrane bound components that facilitate electron transfer from NADPH to oxygen.
84 These two proteins depend on one another for stable expression (Segal, 1987). gp91*phox* is

85 synthesised in the endoplasmic reticulum (ER) as a 58kDa polypeptide. It becomes a 65kDa high
86 mannose precursor, then acquires heme, forms a heterodimer with p22*phox* and is glycosylated in
87 the Golgi apparatus before transport to endosomes (in macrophages) and to peroxidase-negative
88 granules (in neutrophils) or the plasma membrane. The process of heterodimer formation is
89 relatively inefficient and gp91*phox* monomers are rapidly degraded from the ER (DeLeo et al.,
90 2000). Chaperones such as hsp90 (Chen et al., 2011) and hsp70 (Chen et al., 2012) regulate
91 gp91*phox* abundance, as does the negative regulator of reactive oxygen species, NRROS
92 (Noubade et al., 2014). We demonstrated that the protein Essential for Reactive Oxygen Species
93 (EROS, gene symbol *CYBC1*) has profound effects on gp91*phox* and p22*phox* abundance. The
94 heterodimer is essentially absent in EROS deficient cells in both mouse (Thomas et al., 2017) and
95 human (Thomas et al., 2018) immune cells leading to extreme susceptibility to infection. Further,
96 we and others have demonstrated that human EROS deficiency is a novel cause of CGD: OMIM
97 618935 (Thomas et al., 2018, Arnadottir et al., 2018).

98 However, important questions remain, including (i) the exact mechanism by which EROS
99 regulates gp91*phox*-p22*phox* abundance and (ii) whether EROS regulates the expression of other
100 proteins. Both are key questions given that EROS deficiency is associated with severe morbidity
101 and some clinical manifestations not seen in CGD, such as autoimmune haemolytic anaemia
102 (Thomas et al., 2018) and glomerulonephritis (Arnadottir et al., 2018).

103 In this study, we show that EROS co-transfection with gp91*phox* markedly increases gp91*phox*
104 expression in a variety of cell lines, selectively enhancing expression of the immature 58kDa form
105 of the protein and preventing its degradation. EROS can exist in a trimeric complex with gp91*phox*
106 and p22*phox* through direct binding to gp91*phox*. Heme is not required for the interaction of
107 gp91*phox* and EROS. EROS localises at the ER and the perinuclear membrane, interacting with
108 components of the oligosaccharyltransferase complex (OST), consistent with a role early in
109 biosynthesis. We also report the ligand gated ion channel P2X7 as an EROS target. EROS binds
110 directly to and co-immunoprecipitates with P2X7 and other members of the P2X family.
111 Accordingly, P2X7 driven calcium flux, inflammasome activation, and surface receptor shedding

112 are markedly abnormal in EROS-deficient cells with profound effects on both macrophage and T
113 cell physiology. Together, the lack of gp91 $phox$ -p22 $phox$ and P2X7 leads to resistance to
114 influenza A infection.

Results

EROS is a physiological regulator of gp91phox

EROS is essential for expression of the gp91phox-p22phox components of the phagocyte NADPH oxidase in primary human cells. We have previously shown this in patient-derived material but here also introduce an induced pluripotent stem cells (iPS)-derived macrophages rendered deficient in human EROS via CRISPR-Cas9 (Figure 1 - figure supplement 1A). We examined the exact mechanism of action of EROS, asking how it fitted into the canonical model of gp91phox-p22phox biology (Figure 1 – figure supplement 1B). One established method to investigate gp91phox-p22phox biosynthesis and stability is to transfect components of the complex into cells that do not normally express them (Dinauer, 2019). Such reductionist studies have demonstrated the ability of p22phox to stabilise the mature 91kDa form of gp91phox. Co-expression of murine EROS and gp91phox resulted in markedly increased gp91phox expression relative to gp91phox transfection alone in NIH3T3 and COS-7 cells (Figure 1A-B) which are known not to express endogenous p22phox (Yu et al., 1997) as well as in HEK293T cells (Figure 1C) which express some endogenous p22phox. Thus, EROS can increase the expression of mouse gp91phox and can do so in the absence of p22phox.

This result was corroborated using human constructs of EROS, gp91phox and p22phox (Figure 1D-F). In HEK293T cells, co-transfection of human EROS with gp91phox resulted in increased expression of the predominantly lower molecular weight (immature form) of gp91phox (Figure 1D). EROS's ability to enhance the expression of the 58kDa form specifically was maintained when all three of gp91phox, p22phox and EROS were transfected compared to gp91phox and p22phox only (Figure 1E). This effect was also readily observable in non-adherent HEK293-F cells and with different tags placed on EROS and gp91phox (Figure 1 – figure supplement 1C). Similarly, in p22phox-deficient NIH3T3 cells, co-transfection of human EROS with gp91phox enhanced the abundance of the immature 58kDa form (Figure 1 – figure supplement 1D).

These data demonstrate the ability of EROS to increase immature 58kDa gp91phox abundance in the absence of any p22phox in a manner that is, therefore, independent of p22phox's impact on

142 gp91 phox maturation. In contrast to the results above, EROS co-expression with p22 phox did not
143 increase p22 phox expression with either human (Figure 1F) or mouse (Figure 1 – figure
144 supplement 1E) constructs. Thus, the primary effect of EROS protein is on the abundance of
145 gp91 phox , not p22 phox . Given that these two proteins are only stable as a heterodimer (Segal,
146 1987, Dinauer et al., 1990), EROS needs only be a critical regulator of one of them. Of note,
147 EROS expression was normal in gp91 phox deficient cells (Figure 1 – figure supplement 1F).

148 We next examined whether EROS affected stability of the 58kDa form of gp91 phox by using
149 cycloheximide to block *de novo* protein synthesis. The 58kDa protein was prominently stabilised
150 by co-transfection with EROS with less degradation in its presence (Figure 1G, left panel). Hence,
151 densitometry performed on the 58kDa band (Figure 1G, right panel) resulted in a significantly
152 greater area under curve in EROS and gp91 phox co-transfection compared to gp91 phox
153 transfection alone (Figure 1 – figure supplement 1G). The stability of the 65kDa precursor form
154 and the mature gp91 phox were not affected by the presence of EROS (Figure 1G and data not
155 shown).

156 We complemented this co-transfection work by examining PLB985 cells which express high levels
157 of NADPH oxidase components, especially when they are differentiated into a mature neutrophil
158 phenotype. Overexpression of EROS in PLB985 cells resulted in an increase of the abundance of
159 endogenous gp91 phox , particularly the 58kDa form, which is barely detectable in control PLB985
160 cells (Figure 1H). Analysis of gp91 phox expression in differentiated PLB985 cells deficient in
161 p22 phox showed minimal gp91 phox expression but a small amount of the 58kDa form could be
162 observed. The abundance of this immature form can be increased by lentiviral overexpression of
163 EROS or gp91 phox , with highest abundance when both were transduced. Consistent with the
164 absence of p22 phox , the mature glycosylated form is not seen (Figure 1I). Differentiated PLB985
165 cells deficient in EROS also express minimal gp91 phox at baseline. However, the small amount of
166 gp91 phox that can be detected following forced lentiviral overexpression is of both immature and
167 mature forms because these cells are not genetically deficient in p22 phox (Figure 1J).

168 These data emphasize the necessary role of EROS in stabilizing the immature form of gp91 phox

169 in a human hematopoietic cell line, similar to that observed in our reductionist study.

170 ***EROS can associate with the gp91phox-p22phox heterodimer through direct interaction***
171 ***with gp91phox***

172 In our previous work, we showed that FLAG-tagged EROS could immunoprecipitate with
173 gp91phox. Similarly, we found that endogenous gp91phox immunoprecipitated with endogenous
174 EROS in PLB985 cell line (Figure 2- figure supplement 1A). We explored the details of the
175 association between EROS, gp91phox and p22phox using optimised co-immunoprecipitation
176 conditions in HEK293-F cells expressing FLAG-tagged mouse EROS followed by size exclusion
177 chromatography (SEC) to further purify any complexes containing EROS. In cells transfected with
178 EROS-FLAG, gp91phox-GFP and p22phox, EROS co-immunoprecipitated with the partially
179 glycosylated form of gp91phox (Figure 2A). SEC further showed that it could associate with the
180 heme-bound form of gp91phox as evidenced by the co-elution with the heme absorbance peak
181 (Figure 2B). Immunoblotting of SEC eluate detected p22phox indicating that EROS forms a
182 complex with both gp91phox and p22phox (Figure 2C). Notably, inhibiting heme synthesis using
183 succinyl acetone blocked insertion of heme into gp91phox and prevented co-immunoprecipitation
184 with p22phox, but did not prevent the association between EROS and gp91phox (Figure 2D-E).
185 These data suggested that while EROS increases abundance of and stabilises the immature form
186 of gp91phox, it can remain associated with gp91phox as it binds heme and then p22phox. Thus,
187 we asked whether EROS interacts directly with gp91phox. To address this, we utilised the
188 Nanoluc Binary Technology (NanoBiT) complementation reporter system (Dixon et al., 2016). We
189 fused EROS and gp91phox to Large BiT (LgBiT) and Small BiT (SmBiT) subunits of the luciferase
190 at either the N or C-terminus. Constructs were transfected into HEK293T to test various possible
191 combinations (Figure 2 – figure supplement 1B). The LgBiT-EROS and gp91phox-LgBiT
192 constructs paired with the negative control HaloTag-SmBiT (HT-SmBiT) gave signal within the
193 background. Two separate construct pairs, LgBiT-EROS with gp91phox-SmBiT and SmBiT-EROS
194 with gp91phox-LgBiT generated high intensity luminescence within the first 30min of monitoring

live HEK293T cells (Figure 2F). The combination LgBiT-EROS and gp91*phox*-SmBiT encoded in a single vector (BiBiT vector, see methods) where expression of both gp91*phox* and EROS is driven by the same promotor also generated high intensity luminescence (Figure 2 – figure supplement 1C) thereby demonstrating that gp91*phox* and EROS interact directly. This construct, where EROS and gp91*phox* are encoded by a single vector provides a convenient platform to interrogate questions such as the effect of missense mutations in either protein on their binding or whether certain small molecules can disrupt the interaction.

This is further supported by yeast-two hybrid experiments. Using gp91*phox* bait plasmid and EROS prey plasmid, we specifically observed colonies under the selective media without leucine, tryptophan and histidine (see methods) which confirmed the direct interaction between EROS protein and gp91*phox* (Figure 2G, Figure 2 –figure supplement 2H). Confocal microscopy analysis showed that EROS is found in the ER and perinuclear compartment (Figure 2H), colocalising with calnexin and the lamina-associated polypeptide-2 (Lap2; a nuclear membrane marker). This result is consistent with previous literature reporting a nuclear membrane localisation of the uncharacterised protein C17ORF62, which corresponds to human EROS (Korfali et al., 2010). Given the continuity between the nuclear membrane and the ER, these data suggest that EROS acts very early in gp91*phox* biosynthesis.

These findings support a model where EROS directly binds and stabilises the 58kDa gp91*phox* protein, remaining associated with it through heme incorporation and p22*phox* binding. The role of EROS is thus distinct and temporally separated from that of p22*phox*. In the ER, p22*phox* interacts with gp91*phox* after heme has been incorporated and stabilises the partially glycosylated form (Figure 2 – figure supplement 2). Notably, in the HEK293 co-transfection system, we found that human EROS increased expression of NOX1 and NOX4, two close homologues of gp91*phox* (NOX2). For NOX1, NOX2 and NOX4, this process was not impaired by succinyl acetone treatment (Figure 2 – figure supplement 1D-F). EROS was not able to increase NOX5 expression, which is structurally different to NOX1, 2, 4 (Figure 2 – figure supplement 1G). A further yeast 2 hybrid experiment, using a separate method, as described in (Luck et al., 2020) demonstrated

222 direct binding of EROS to NOX2-3-4 but not NOX5 or p22*phox* (Figure 2 – figure supplement 2H).
223 However, western blot analysis of whole kidney and heart lysate from EROS knockout mice
224 showed no difference in nox4 expression in EROS knockout relative to control (Figure 2- figure
225 supplement 1I). Thus, EROS does not regulate nox4 physiologically in the kidney and heart. We
226 also assayed colon from control and EROS knockout mice for nox1 expression using the highly
227 specific antibody described in Diebold et al. (Diebold et al., 2019). We did not see a difference in
228 expression between control and EROS knockout mice (Figure 2- figure supplement 1I). Non-
229 specific bands were seen with EROS antibody (which is common in mouse lysates) but we could
230 not detect EROS band which is consistent with its low expression level in these tissues.
231 Nevertheless, our co-transfection and yeast two hybrid data may provide important clues to the
232 motifs that EROS recognises in directly binding NOX proteins.

233 ***EROS-mediated regulation of gp91*phox* and the OST complex***

234 The ability of EROS to act at the earliest stage of gp91*phox* biosynthesis prompted us to examine
235 its biology in greater detail. To identify EROS-associated proteins we performed 4 biological
236 replicate FLAG affinity purifications from both RAW 264.7 macrophages overexpressing FLAG-
237 tagged EROS and untagged control cells (Thomas et al., 2017). We used the widely adopted
238 statistical algorithm Significance Analysis of INteractome (SAINTexpress; (Teo et al., 2014)) to
239 discriminate specific EROS interactors from non-specific or background binders. SAINTexpress
240 uses quantitative information from the mass spectrometry data, more specifically the abundance of
241 each identified protein in the bait experiments compared to the control purifications, to score the
242 probability of a true interaction. The SAINT probability (SP) score represents the confidence level
243 of potential protein interactions, with 1 being the highest possible value. We applied a stringent
244 threshold of SP>0.9 (False Discovery Rate<1%) to derive a list of 59 high confidence EROS
245 interactors (Figure 3A). Network analysis using STRING interaction database showed that the
246 majority of these proteins were connected between them through physical interactions (Figure 3B).
247 Gene ontology (GO) enrichment analysis revealed “N-linked glycosylation” as one of the most

248 enriched terms in our EROS-interacting protein set, and “positive regulation of glycoprotein
249 biosynthetic process” was also enriched. High confidence EROS interactors
250 oligosaccharyltransferase 48kDa subunit (DDOST/OST48), ribophorin-1 (RPN1) and ribophorin 2
251 (RPN2) form the non-catalytic subunit of the oligosaccharyltransferase (OST) complex (Pfeffer et
252 al., 2014). Staurosporine and temperature sensitive 3A (STT3A), which forms the catalytic subunit
253 of the OST complex (Ramirez et al., 2019) was specifically identified in three out of four EROS
254 pull-down experiments and not in controls, although it did not make the strict SP score cut-off,
255 suggesting it might also be an EROS interactor. These data point to EROS being bound to
256 gp91*phox* while N- glycosylation takes place.

257 Translation, synthesis and N-glycosylation of proteins transferred into the ER involve the ER
258 translocon-machinery comprising the SEC61 channel, the translocon-associated protein (TRAP)
259 complex and the OST complex responsible for the addition of N-linked oligosaccharides to
260 nascent protein (Cherepanova et al., 2016). We hypothesized that EROS may cooperate with the
261 OST complex to facilitate the stabilization and maturation of gp91*phox*. HEK293 cells expressing
262 STT3A-GFP and EROS-mRFP constructs exhibited an ER localization of the two proteins with a
263 specific rim around the nucleus (Figure 3C, right panel). Quantitation of the pixel intensity of
264 STT3A-GFP and EROS-mRFP across the nuclear membrane gave an identical profile (Figure 3C,
265 left panel). Similarly, co-expression of STT3A-GFP, gp91*phox*-mRFP and EROS untagged
266 constructs lead to an ER and perinuclear localization of the three proteins (Figure 3D, right panel)
267 with an identical pixel intensity profile upon quantitation (Figure 3D, left panel). These data
268 demonstrate that a proportion of gp91*phox* can be found at the site of STT3A and EROS
269 localization. Inhibition of the OST complex with the selective compound NGI-1 (Puschnik et al.,
270 2017, Rinis et al., 2018) impaired the ability of EROS to increase the immature 58kDa form in a
271 dose-dependent manner (Figure 3E) in HEK293 cells.

272 To complement these findings, we expressed the gp91*phox* construct alone or in combination
273 with the EROS construct in HEK293 deficient in *STT3A* or *STT3B* (Cherepanova and Gilmore,
274 2016). STT3A interacts directly with SEC61 and mediates co-translational N-glycosylation. STT3B,

275 is not associated with SEC61, and glycosylates sites skipped by STT3A. In the absence of STT3A,
276 we observed a shift in the glycosylation pattern of gp91 phox compared to control conditions,
277 resulting in an increase of the immature 58kDa form (Figure 3F). Co-expression of gp91 phox with
278 EROS in $\text{STT3A}^{-/-}$ cells resulted in the same effect with the appearance of further bands around
279 65kDa, probably glycosylation intermediates. $\text{STT3B}^{-/-}$ cells, instead, exhibited an overall increase
280 of gp91 phox abundance compared to control cells both in the absence or presence of EROS
281 (Figure 3F). These glycosylation intermediates were suppressed by treatment of $\text{STT3A}^{-/-}$ cells
282 expressing gp91 phox and EROS with the inhibitor NGI-1, leaving only the 58kDa band (Figure 3-
283 figure supplement 1A). The 58kDa band was not detectable in cells treated with the compound
284 tunicamycin, a widely used N-glycosylation inhibitor. The overall increase of gp91 phox abundance
285 in $\text{STT3B}^{-/-}$ cells in presence of EROS was also impaired by treatment with NGI-1 (Figure 3- figure
286 supplement 1A). Interestingly, NGI-1 treatment of PLB985 cells also shifted the glycosylation
287 pattern of gp91 phox , selectively enhancing bands at 65kDa and 58kDa form compared to DMSO
288 treatment where we observed a predominantly mature 91kDa protein (Figure 3G). This suggests
289 that blockade of the OST machinery in the ER prevents subsequent proper glycosylation in the
290 Golgi apparatus. Lack of STT3A as well as treatment with NGI-1 led to an increase in the
291 expression of the ER stress marker BiP in HEK293 and in PLB985 cells (Figure 3- Figure
292 supplement 1B-D). This finding is recapitulated by treatment of PLB985 cells with tunicamycin
293 (Figure 3 – Figure supplement 1D).

294 Overall, these findings are consistent with EROS being bound to gp91 phox at the early stages of
295 its biosynthesis while N-glycosylation takes place in ER. They also reveal a previously
296 unappreciated involvement of the OST complex in gp91 phox maturation process stressing a
297 requirement of the catalytic subunit STT3A in the co-translational glycosylation of gp91 phox .

298 ***EROS targets a specific group of proteins***

299 Having defined the role of EROS in gp91 phox -p22 phox heterodimer maturation, we leveraged
300 new artificial intelligence tools to gain insights into its structure. The structure of the full-length
301 EROS protein predicted by AlphaFold 2.0 (Jumper et al., 2021) is available through the AlphaFold

Protein Structure Database (Tunyasuvunakool et al., 2021). The predicted structure shows a tripartite organisation of (i) a PH domain, (ii) an integral membrane segment and (iii) a flexible C-terminal tail (Figure 4A). The EROS protein contains a Pleckstrin Homology (PH) domain composed of residues 1 to 20 (containing beta strands 1 and 2) and residues 62 to 166 (containing beta strands 3 to 8 and alpha helices H3 and H4). Inserted between beta strands 2 and 3 of the PH domain are two integral membrane alpha helices (helices H1 and H2) that are packed in an antiparallel orientation. The C-terminal tail of EROS composed of residues 167 to 187 has a structure with very low confidence <50 pLDDT (predicted local Distance Difference Test) which is usually indicative of disordered regions of proteins. Multiple independent models built with AlphaFold (data not shown) show a wide variety of conformations for this tail confirming its lack of regular structure. If confirmed experimentally, the insertion of transmembrane helices within a PH domain appears to be a hitherto unobserved feature within known structures. A similar PH domain organization is predicted to be found in the structure of the Phosphatidylinositol Glycan Anchor Biosynthesis class H (PIGH) protein (UniProtKB-Q5M9N4). This ER-associated transmembrane protein is part of the glycosylphosphatidylinositol-N-acetylglucosaminyltransferase (GPI-GnT) complex that catalyses the transfer of N-acetylglucosamine from UDP-N-acetylglucosamine to phosphatidylinositol and participates in the first step of GPI biosynthesis. GPI is an anchor for many membrane proteins, including key immune proteins such as the receptors CD16 and CD14 (Wegner et al., 2021) as well as the complement regulatory proteins CD55 and CD59 (Tremblay-Laganiere et al., 2021). Therefore, we asked whether EROS might regulate the abundance of other proteins in different immune cell types.

We performed Tandem Mass Tagging proteomics analysis on bone marrow derived macrophages (BMDM) and CD4 T cells from control and EROS knockout mice. This approach allowed the identification of around 8000 proteins, a greater number than our previously reported label-free experiment which was limited to 2000 proteins (Figure 4B, C). We found that EROS deficiency has major effects on the expression of a small number of proteins in macrophages and this effect is conserved in CD4 T cells. These proteins were gp91*phox* (*Cybb*), p22*phox* (*Cyba*) and P2x7, the

329 latter also identified as a high confidence EROS-interacting protein (see Figure 3A). Additionally,
330 we observed a lower expression of the tumour suppressor protein Phactr4 (Solimini et al., 2013) in
331 EROS-deficient cells. Phactr4 plays a key role in actin cytoskeleton remodelling by regulating the
332 β 1 integrin–FAK–ROCK-cofilin pathway (Huet et al., 2013, Sun and Fassler, 2012). The
333 immunological role of Phactr4 is currently unknown.

334 Given that EROS seemed to affect proteins that localised to the plasma membrane, we performed
335 plasma membrane profiling analysis to determine whether evaluating this compartment alone
336 might reveal more proteins regulated by EROS. This analysis demonstrated very similar results.
337 gp91*phox*, p22*phox* and P2x7 were the most down-regulated proteins in EROS-deficient cells
338 compared to control cells. The sodium/proton exchanger Slc9a9 was significantly up-regulated
339 (Figure 4D).

340 Thus, the biological effects of EROS deficiency are conserved across different immune cells and it
341 targets a very selective group of transmembrane proteins.

342 ***EROS regulates the abundance of the P2X7 ion channel in mouse and human cells***

343 The purinergic receptor P2X7 was consistently downregulated in all our mass spectrometry data
344 ((Thomas et al., 2017), Figure 4) of EROS-deficient cells and was identified as a confident EROS
345 interactor (Figure 3A). Proteins including Elmo1, Dock2 and mTOR (Figure 3B) are also confident
346 EROS interactors but their expression remained unchanged in EROS-deficient cells (Figure 4B-C).

347 Thus, P2X7 seems the only confident EROS interactor (Figure 3A-B) whose expression is
348 regulated by EROS similarly to gp91*phox*. Therefore, we focused on validating EROS's role in
349 controlling P2X7 abundance. We verified this by western blot (Figure 5A) and flow cytometry of
350 both BMDM (Figure 5 – figure supplement 1A) and freshly isolated peritoneal macrophages
351 (Figure 5 – figure supplement 1B) in independent cohorts of mice. The lack of P2X7 in EROS-
352 deficient cells was not a consequence of lack of expression of the NADPH oxidase as P2X7
353 protein was expressed normally in gp91*phox*-deficient cells (Figure 5B). Consistent with our mass
354 spectrometry data (Figure 4B), P2X7 expression was extremely low on CD4⁺ T cells from EROS

355 knockout mice, measured by western blot and flow cytometry (Figure 5 – figure supplement 1C-D).

356 Control splenocytes had high levels of P2X7 expression in NKT cells and $\gamma\delta$ T cells with much

357 reduced expression in EROS-deficient cells (Figure 5 – figure supplement 1E-F). EROS deficiency

358 also led to reduced P2X7 expression in B cells, NK cells and CD8⁺ T cells (Figure 5 – figure

359 supplement 1G, 1H, 1I).

360 P2X7 was very lowly expressed in human iPS-derived macrophages (Figure 5C) and PLB-985

361 cells (Figure 5D) that carried a CRISPR mediated deletion in EROS. RAW264.7 macrophages

362 express P2X7 endogenously and lentiviral overexpression of EROS increased P2X7 expression

363 relative to that observed with a control vector that expressed only GFP (Figure 5E). This effect

364 was reproduced in HEK293 cells. Co-transfection of EROS and P2X7 resulted in much higher

365 expression of P2X7 than when P2X7 was transfected alone (Figure 5F, Figure 5 – figure

366 supplement 1J). Therefore, not only does EROS deficiency led to a lack of P2X7 expression, but

367 EROS up-regulation increased P2X7 abundance. We hypothesised that the regulation of P2X7

368 abundance would have a similar mechanism to that for the gp91*phox*-p22*phox* heterodimer.

369 Accordingly, P2X7 co-immunoprecipitated with EROS from RAW264.7 macrophages that

370 expressed an N-terminal FLAG-tagged EROS (Figure 5G). Furthermore, NanoBiT analysis using a

371 LgBiT-EROS and P2X7-SmBiT pair constructs in HEK293 resulted in luminescence production

372 showing that the interaction between P2X7 and EROS was direct (Figure 5H).

373 Macrophages express other P2X family members including P2X4 and P2X1 (Sim et al., 2007).

374 Western blot analysis of BMDM also demonstrated a lower expression of P2X1 in EROS-deficient

375 cells (Figure 5I). As with P2X7, co-transfection of both P2X1 and EROS caused greater

376 expression of P2X1, compared to when P2X1 was transfected alone (Figure 5J). Thus, EROS also

377 regulates P2X1 protein abundance. This was not, however, the case for P2X4 (Figure 5 – figure

378 supplement 1K) which is mainly found in endolysosomal compartment in macrophages

379 (Boumechache et al., 2009, Robinson and Murrell-Lagnado, 2013). These data emphasise the

380 role of EROS in selectively controlling P2X7 expression through a direct recruitment analogous to

381 that observed for gp91*phox*.

382 ***Loss of P2X7 impairs inflammasome activation and shedding of surface ligand.***

383 P2X7 is a metabotropic ion channel and ligation by adenosine-5'-triphosphate (ATP) is associated
384 with an inward flux of calcium and sodium an outward flux of potassium ions (Bartlett et al., 2014).
385 We measured calcium influx following treatment of control and EROS-deficient BMDM by 2'(3')-O-
386 (4-Benzoylbenzoyl)ATP (bzATP), which has higher affinity than ATP for the P2X7 receptor. bzATP
387 driven calcium flux was highly attenuated in EROS-deficient macrophages compared to their
388 control counterpart (Figure 6A). Ionomycin driven responses were equivalent between the two
389 strains, showing that there was no inherent problem with calcium mobilisation in EROS deficiency
390 (Figure 6A). Ligation of P2X7 by ATP is a key mediator of IL-1 β production via the NOD-, LRR-
391 and pyrin domain-containing protein 3 (NLRP3) inflammasome (de Torre-Minguela et al., 2016).
392 Lipopolysaccharide (LPS) treatment alone of the peritoneal macrophages from control and EROS
393 knockout mice resulted in the secretion of modest amounts of IL-1 β . Robust induction of IL-
394 1 β secretion was observed upon treatment of the LPS-conditioned macrophages with ATP and
395 this was approximately 4-fold lower in EROS-deficient cells (Figure 6B). The requirement of EROS
396 for P2X7-mediated calcium uptake and IL-1 β production was previously reported in an
397 independent study (Ryoden et al., 2020). In our *in vivo* data following intraperitoneal LPS and ATP
398 injection, peritoneal washings from EROS knockout mice showed much reduced IL-1 β secretion
399 compared with control (Figure 6C). Consequently, caspase-1 activation was highly attenuated in
400 EROS-deficient macrophages following LPS/ATP treatment (Figure 6D) compared to control
401 macrophages. LPS treatment, either *in vitro* or *in vivo*, resulted in comparable levels of TNF- α , IL-
402 10, IL-6 and KC/GRO secretion between control and EROS-deficient macrophages and levels of
403 these cytokines were not altered significantly by ATP addition (Figure 6 – figure supplement 1A-F).
404 P2X7 plays several important roles in CD4⁺ T cell biology, including ADAM10/17 driven shedding
405 of cell surface molecules such as CD62L and CD27 and externalisation of phosphatidylserine
406 (PS), pore formation and cell death (Bartlett et al., 2014, Scheuplein et al., 2009). Accordingly,
407 flow cytometry analysis of CD62L level following ATP treatment showed reduced staining in

control CD4⁺ T cells with 10% of cells positive for CD62L-APC compared to 70% of positive cells pre-ATP addition (Figure 6E). In EROS-deficient CD4⁺ T cells, this ATP driven CD62L shedding is significantly impaired (Figure 6E). Similar results were obtained when examining CD27 shedding (Figure 6F). Nicotinamide adenine dinucleotide (NAD)-driven shedding of CD62L and CD27 was also significantly decreased in EROS-deficient CD4⁺ T cells albeit to a lesser extent than with ATP treatment (Figure 6 – figure supplement 1G-H). PS exposure and cell death, assessed by annexin V and propidium iodide staining, were reduced in EROS-deficient CD4⁺ T cells following ATP treatment (Figure 6G) consistent with published findings (Ryoden et al., 2020). We speculated that there might be further *in vivo* consequences to the loss of both P2X7 and phagocyte NADPH oxidase activity in EROS knockout mice and noted that blockade of the P2X7 receptor has been associated with improved outcomes in influenza A virus (IAV) infection (Snelgrove et al., 2006, Leyva-Grado et al., 2017, Rosli et al., 2019). We intranasally injected control and EROS knockout mice with IAV and found that EROS knockout mice were protected from infection with a 50-60% reduction in mortality (Figure 6H). These results identify a central role of EROS in modulating purinergic signalling *in vivo* through targeting P2X7.

424 Discussion

425 Cytochrome b558 is essential for defence against infection and a key modulator of inflammatory
426 pathways. gp91*phox* exists as a co-dependent heterodimer with p22*phox* (Segal, 1987).
427 gp91*phox* is translated as a 58kDa immature protein which undergoes successive post-
428 translational modifications leading to the association with p22*phox* and final maturation to a
429 functional 91kDa protein (DeLeo et al., 2000). The 58kDa form is inherently much more unstable
430 and prone to proteasomal degradation than the mature 91kDa form, as we also observed in this
431 study. Recently, we showed that another protein, EROS, was essential for the expression of both
432 gp91*phox* and p22*phox*. EROS deficiency led to a lack of gp91*phox* and p22*phox*, (Thomas et al.,
433 2017, Thomas et al., 2018) raising the question of how it fits into the canonical model above. Our
434 study offers several new insights compared to previous work.

435 We show, by two different techniques, that EROS binds gp91*phox* directly and is needed very
436 early in gp91*phox* biogenesis, in contrast to p22*phox*, preferentially stabilising the gp91*phox*
437 58kDa precursor before heme incorporation takes place. Much work has been done to
438 characterise the latter stages of gp91*phox* maturation (Porter et al., 1996, Yu et al., 1997, Yu et
439 al., 1999, DeLeo et al., 2000, Beaumel et al., 2014). This study offers unique insight into the early
440 stages of the protein's biosynthesis, on which all subsequent events depend. These early stages
441 involve the OST-complex, which is required for the initial glycosylation events, folding and
442 insertion into the ER membrane (Gemmer and Forster, 2020). The OST complex adds a
443 preformed oligosaccharide to an asparagine residue on a newly synthesized protein (Cherepanova
444 et al., 2016). Murine gp91*phox* has one asparagine residue while human gp91*phox* has three
445 asparagine residues that are glycosylated (Harper et al., 1985, Wallach and Segal, 1997). Using
446 PNGaseF and EndoH-treated lysates as a reference, we demonstrated that EROS
447 immunoprecipitated with partially glycosylated gp91*phox*. Blockade of OST-mediated N-
448 glycosylation, through chemical inhibition or use of cells lacking the catalytic subunit STT3A,
449 impacts on the gp91*phox* glycosylation pattern upon co-transfection with EROS in HEK293 cells
450 but does not reduce the abundance of gp91*phox* *per se* as does EROS deficiency. Hence, we

451 propose that EROS works post-translationally, stabilizing gp91*phox* so that the high mannose
452 precursor can be synthesized and undergo further maturation.

453 We find that EROS can increase the abundance of NOX1, gp91*phox* (NOX2) and NOX4 in co-
454 transfection assays and that it can directly bind NOX2, NOX3 and NOX4 in yeast-2-hybrid assays.
455 This contrasts with its inability to augment the expression of NOX5 or p22*phox* and suggests that
456 EROS likely binds a conserved motif in those NOX proteins that depend on p22*phox* for stability.

457 We also present an EROS deficient iPS-derived human macrophage line. This recapitulates the
458 effects seen in cell lines and patients for gp91*phox*-p22*phox* but demonstrates for the first time in
459 a primary human cell that EROS deficiency leads to P2X7 deficiency and that this is likely an
460 important part of the human syndrome.

461 We place the role of EROS in context by using a granular mass spectrometry detecting up to 8000
462 proteins in different cell types to clearly define the range of proteins that EROS can regulate in
463 context of the entire proteome. We used both whole cell and plasma membrane to show just how
464 specific EROS is in its physiological effects. In addition to our work on human iPS-derived
465 macrophages, we make new insights into the biology of the control of P2X7 expression by EROS.

466 The effects of EROS deficiency on P2X7 expression were noted in our original mass spectrometry
467 analysis and in a recent screen of factors that influence ATP driven phosphatidylserine excursion
468 (Ryoden et al., 2020). In this work, we show that EROS knockout mice have P2X7 deficiency in
469 eight primary cell types of the murine immune system. Several splice variants exist in different
470 tissues and it is important to clarify whether EROS has cell type specific effects on P2X7
471 expression. Notably in our T cell experiments, EROS-driven P2X7 deficiency affects shedding of
472 CD27 and CD62L and ATP-driven cell death. Moreover, we show that the effects on P2X7 are a
473 class effect with similar, but more modest, effects on P2X1 expression. We demonstrate that the
474 mechanism by which this occurs is a direct effect on P2X7 and, by extension, is likely to be a
475 direct effect on P2X1. Significantly, EROS overexpression drives increased abundance of P2X7
476 and P2X1, suggesting that EROS might act as a physiological regulator of purinergic signalling.

477 A particular strength of our study is that we show marked *in vivo* sequelae of the lack of P2X7.

478 EROS deficiency leads to profound susceptibility to bacterial infection but protects mice from
479 infection with influenza A. This is likely to reflect the fact that mice that are (i) deficient in
480 gp91 ϕ ox, (ii) deficient in P2X7, (iii) treated with P2X7 inhibitors have improved outcomes
481 following infection with influenza A and raises intriguing questions about the physiological role of
482 EROS. Snelgrove et al. showed that gp91 ϕ ox deficiency improved outcomes in influenza A.
483 gp91 ϕ ox knockout mice exhibited a reduced influenza titre in the lung parenchyma. Inflammatory
484 infiltrate into the lung parenchyma was markedly reduced and lung function significantly improved
485 (Snelgrove et al., 2006). To et al. then demonstrated that the phagocyte NADPH oxidase is
486 activated by single stranded RNA and DNA viruses in endocytic compartments. This causes
487 endosomal hydrogen peroxide generation, which suppresses antiviral and humoral signalling
488 networks via modification of a highly conserved cysteine residue (Cys98) on Toll-like receptor-7. In
489 this study, targeted inhibition of endosomal ROS production using cholestanol-conjugated
490 gp91dsTAT (Cgp91ds-TAT) abrogates influenza A virus pathogenicity (To et al., 2017). This group
491 went on to explore infection with a more pathogenic influenza A strain, PR8 using the same
492 specific inhibitor. Cgp91ds-TAT reduced airway inflammation, including neutrophil influx and
493 alveolitis and enhanced the clearance of lung viral mRNA following PR8 infection (To et al., 2019).
494 This group has also shown that NOX1 (Selemidis et al., 2013) and NOX4 (Hendricks et al., 2022)
495 can drive pathogenic inflammation in influenza A, emphasising the importance of clarifying the
496 roles of EROS in control of expression of these proteins.

497 In studies on P2X7, Rosli et al. found that mice infected with 10⁵ PFU of influenza A HKx31 had
498 improved outcomes if they were treated with a P2X7 inhibitor at day 3 post infection and every two
499 days thereafter. Survival was also improved even if the inhibitor is given on day 7 post infection
500 following a lethal dose of the mouse adapted PR8. This was associated with reduced cellular
501 infiltration and pro-inflammatory cytokine secretion in bronchoalveolar lavage fluid, but viral titres
502 were not measured (Rosli et al., 2019). Leyva-Grado et al. examined influenza A infection in P2X7
503 knockout mice. They infected mice with both influenza A/Puerto Rico/08/1934 virus and influenza
504 A/Netherlands/604/2009 H1N1pdm virus. They showed that P2X7 receptor deficiency led to

505 improved survival after infection with both viruses with less weight loss (Leyva-Grado et al., 2017).
506 Production of proinflammatory cytokines and chemokines was impaired and there were fewer
507 cellular hallmarks of severe infection such as infiltration of neutrophils and depletion of CD11b⁺
508 macrophages. It is worth noting that the P2X7 knockout strain used in this study was the Pfizer
509 strain in which some splice variants of P2X7 are still expressed (Bartlett et al., 2014). Hence, the
510 dual loss of the phagocyte NADPH oxidase and P2X7 in EROS knockout mice likely confers
511 protection from IAV infection. By reducing the expression of both NOX2 and P2X7, EROS
512 regulates two pathways that may be detrimental in influenza A and we speculate that EROS may
513 physiologically act as a rheostat controlling certain types of immune response.

514 P2X7 is crucial for ATP driven activation of the NLRP3 inflammasome and has an emerging role in
515 T cell biology, especially in resident immune cells (Stark et al., 2018). Of note, P2X7 ligation by
516 ATP is also a potent driver of ROS formation, the other major process that is profoundly affected
517 by EROS deficiency (Pfeiffer et al., 2007). One role of EROS might be to modulate ATP driven
518 danger signalling including ROS and NLRP3 activation through controlling the biosynthesis of
519 NOX2 and P2X7. Both ROS and NLRP3 activation are clearly essential but the extent and
520 duration of responses must be controlled to limit tissue damage. Therefore, one might consider
521 EROS as a rheostat for these key linked immune processes.

522 In conclusion, we have elucidated the mechanism by which EROS controls the abundance of
523 gp91 ϕ ox and purinergic receptors and defined EROS as a highly selective molecular chaperone
524 that can shape immune responses through targeting specific proteins. As well as advancing our
525 understanding of the physiology of highly conserved and non-redundant proteins, this work has
526 implications for translational medicine, including gene therapy and possible therapeutic blockade
527 of EROS to limit viral immunopathology.

528 **Methods**

529 *Animal use:*

530 EROS/*Cybc1*^{-/-} mice (KOMP) and gp91*phox*/*Cybb*^{-/-} mice were previously described (Thomas et
531 al., 2017). The care and use of all mice were in accordance with UK Home Office regulations (UK
532 Animals Scientific Procedures Act 1986). The mice were maintained in specific pathogen-free
533 conditions and matched by age and sex within experiments. For the mouse infection, groups of
534 >15 isofluorane-anaesthetised mice of wild type or EROS knockout genotype were intranasally
535 inoculated with 3.10³ PFU of A/X-31 influenza in 50µl of sterile PBS. Their weight was recorded
536 daily and they were monitored for signs of illness. Mice exceeding 25% total weight loss were
537 killed in accordance with UK Home Office guidelines.

538 *DNA constructs*

539 Untagged pEGBacMam-p22*phox* was amplified from OHu21427 (GenScript) by PCR and
540 subcloned in pEGBacMam vector, a kind gift from Eric Gouaux (Oregon Health & Science
541 University; (Goehring et al., 2014)) using In-Fusion seamless DNA cloning (Takara Bio). PCR was
542 used to generate the pEGBacMam-Strep-FLAG-Strep-EROS construct, by amplifying the human
543 EROS/*CYBC1* gene and contextually inserting the Strep-FLAG-Strep tag at its 5'. Human NOX1
544 was synthesised by Genewiz with a Strep II-FLAG tag at the N-terminus and cloned into the
545 pEGBacMam vector using In-Fusion seamless DNA cloning (Takara Bio). The cDNAs encoding
546 for human NOX5 (isoform b) was synthesized by GeneArt and subcloned into the pNGFP-EU
547 vector, a kind gift from Eric Gouaux (Kawate and Gouaux, 2006).

548 *Cell line culture*

549 HEK293T, HEK293, control HEK293, *STT3A*^{-/-} HEK293, *STT3B*^{-/-} HEK293, COS-7, NIH/3T3, and
550 RAW 264.7 EROS FLAG-tagged cells were maintained in DMEM medium (21969035,
551 ThermoFisher) containing 10% FBS (F7524, Sigma-Aldrich) and 100U/mL of Penicillin-
552 Streptomycin-Glutamine (10378016, ThermoFisher). PLB985 (ACC 139, DSMZ), PLB-clone 14
553 (Thomas et al., 2018), PLB- clone 20 (Thomas et al., 2018) and PLB985 overexpressing EROS-
554 GFP lentivirus construct were cultured in complete RPMI medium consisting of RPMI 1640

555 (31870025, ThermoFisher), 10% FBS (F7524, Sigma-Aldrich), 2mM GlutaMAX (35050061,
556 ThermoFisher), 1mM sodium pyruvate (11360070, ThermoFisher); 0.5mg/mL Penicillin-
557 Streptomycin-Glutamine (10378016, ThermoFisher) and 20mM HEPES (H3537, Sigma-Aldrich).
558 HEK293-F cells were grown in suspension using FreeStyle medium (Invitrogen). All cell lines were
559 tested and confirmed mycoplasma-free using the protocol for Myco-Alert- Mycoplasma Detection
560 Kit (LT07-218, Lonza).

561 *Primary cell culture*

562 To generate bone marrow derived macrophages, bone marrow cells harvested from femurs and
563 tibias of 6–10-week-old control or EROS knockout mice were grown in complete RPMI medium
564 supplemented with 100 ng/mL of murine M-CSF (Peprotech) for 3 days. At day 3, 10 mL of the
565 same medium was added to the culture and differentiated macrophages were collected at day 7
566 for mass spectrometry or western blot analysis. To isolate mouse CD4 lymphocytes, mouse
567 spleens were homogenised by manual disruption and subjected to positive selection using CD4
568 L3T4 magnetic beads (Miltenty Biotech) according to the manufacturer's protocol. Cells were
569 counted and resuspended at a concentration of 2×10^6 cells per ml in complete RPMI medium for
570 subsequent analysis.

571 Control or EROS-deficient human induced pluripotent stem cells (iPS) were generated by CRISPR
572 Cas 9-targeted deletion of 46 base pairs in exon 5 of the *CYBC1* sequence (Yeung et al., 2017).
573 Human macrophages were obtained from the differentiation of the human control or EROS-
574 deficient iPS line following previously established method (van Wilgenburg et al., 2013, Thomas et
575 al., 2017). Macrophages were cultured in complete RPMI in presence of human M-CSF
576 (Peprotech) and were used at day 7 post-differentiation.

577 *Transient expression*

578 Cells were transfected at 60-80% confluency with 1.6µg-2µg of the following constructs: mouse
579 gp91*phox*, mouse GFP-tagged gp91*phox*, mouse EROS, human EROS, human gp91*phox*,
580 human mRFP-tagged gp91*phox*, human p22*phox*, human NOX4, mouse GFP-tagged P2X7,
581 human P2X1 and human P2X4; using Lipofectamine RNAiMAX (Thermo Fisher) reagent for

582 HEK293T, HEK293 and COS-7 cells and Lipofectamine 2000 (Thermo Fisher) reagent for NIH3T3
583 cells, following the manufacturer's recommendation. HEK293-F were transfected with
584 polyethylenimine (Polyscience Europe GmbH) at a ratio of 1:3 DNA:polyethylenimine (Tom et al.,
585 2008), using 0.5µg of the indicated constructs. Equivalent amounts of the corresponding empty
586 vector were used as negative control. Cells were harvested and analysed 48h-72h post-
587 transfection.

588 *Protein stability and drug treatment*

589 For cycloheximide experiment, HEK293T cells (transfected with a gp91*phox* construct alone or in
590 combination with an EROS construct) and PLB985 cells (parental and expressing lentivirus
591 EROS-GFP), were treated with 10µg/mL of cycloheximide (Sigma) and harvested at 2h, 4h, 6h
592 and 8h post-treatment and subjected to western blot. Non-treated cells were used as control. For
593 heme synthesis inhibition, 10µg/mL succinyl acetone (Merck) was added to the cell culture 4h
594 after transfection. For glycosylation inhibition, NGI-1 compound (TOCRIS) or tunicamycin (Sigma)
595 was added 3h post-transfection of HEK293 cells and left until harvesting (48h-72h later).

596 *Immunoprecipitation and Size exclusion Chromatography*

597 Strep tagged-EROS was co-transfected in HEK293-F cells with GFP-gp91*phox* and p22*phox*. 48h
598 post transfection cells were harvested and cell membranes were prepared as described in Ceccon
599 et al., (Ceccon et al., 2017). Membranes were solubilised with 1% LMNG in 50mM Hepes pH 7.5,
600 100mM NaCl, 20% (v/v) glycerol, and passed through Streptactin-resin. Bound proteins were
601 eluted from the column with 5mM desthiobiotin in 50mM Hepes pH 7.5, 100mM NaCl, 5% (v/v)
602 glycerol and then subjected to size exclusion chromatography using a Superose 6 30/150 column.
603 Lysates from $3 \cdot 10^7$ to $4 \cdot 10^7$ of cells were subjected to immunoprecipitation according to
604 manufacturer's protocol for the Sure Beads Protein G Magnetic Beads (161-4023, Biorad) using a
605 rat anti-FLAG antibody (Biolegend), the mouse anti-gp91*phox* antibody (Santa Cruz) and an
606 IgG2aK isotype control antibody (14-4321-82, Invitrogen). Eluates from FLAG, gp91*phox* and IgG
607 control beads were analysed by western blotting. Where indicated, lysates were treated with
608 PNGase F or EndoH (New England Biolabs) following manufacturer's recommendation.

609 *Western blot analysis*

610 Cells were lysed at a concentration of 2×10^7 cells per mL in Pierce RIPA buffer (89900,
611 ThermoFisher) containing cOmplete Protease Inhibitor Cocktail (11697498001, Sigma Aldrich)
612 and Halt Protease and Phosphatase inhibitor (78440, Thermo Fisher). Protein concentration was
613 determined by BCA assay (23225, Thermo Fisher) according to manufacturer's instructions. 15 to
614 20µg of protein, mixed with 4X NuPage sample buffer (NP0008, Thermo Fisher), were resolved on
615 a NuPAGE 4-12% Bis-Tris gel (NP0336BOX; NP0335BOX; Thermo Fisher) under reducing
616 conditions in MOPS buffer (mops-sds1000, Formedium), transferred to a nitrocellulose membrane
617 (GE10600003, Sigma-Aldrich) in NuPage transfer buffer (NP00061; ThermoFisher), and probed
618 with one of the following primary antibodies: mouse anti-gp91 phox (Santa-Cruz Biotechnology),
619 rabbit anti-C17ORF62/EROS (Atlas), rabbit anti-p22 phox (Santa-Cruz Biotechnology), mouse anti-
620 p22 phox (Santa-Cruz Biotechnology), rabbit anti-P2X1 (Alomone), rabbit anti-P2X4 (Alomone),
621 rabbit anti-P2X7 (Alomone; Atlas), rabbit anti-P2X7 (Atlas Antibodies), rabbit anti-vinculin (Cell
622 Signalling Technology), rabbit anti-actin (Abcam), mouse anti- α -tubulin (Abcam), mouse anti-
623 FLAG-M2 (Sigma), a homemade rat anti-NOX1 antibody given by Dr. Misaki Matsumoto and a
624 rabbit anti-NOX4 antibody from Prof. Ajay Shah (Kings College London, UK). Secondary
625 antibodies used were anti-rabbit IgG-horseradish peroxidase (7074S, Cell Signaling Technology,
626 dilution 1:10000), anti-rat IgG-horseradish peroxidase (62-9520, Thermo Fisher, dilution 1:5000)
627 and anti-mouse IgG-horseradish peroxidase (7076S, Cell Signaling Technology, dilution 1:10000).
628 Blots were developed using one of the following: ECL (32106, Thermo Fisher), SuperSignal West
629 Pico PLUS (34577, Thermo Fisher) or SuperSignal West Femto (34095, Thermo Fisher) reagents
630 and chemiluminescence was recorded on a ChemiDoc Touch imager (BioRad).

631 *NanoBiT assay for protein-protein interaction*

632 The assay was performed following manufacturer's protocol for the MCS Starter System (N2014,
633 Promega). The constructs encoding EROS/CYBC1 or gp91 phox /CYBB fused to the reporter
634 subunits were custom made by Promega and consist of the following: SmBiT-CYBC1 (TK) vector

635 (CS1603B224), *CYBC1*-SmBiT (TK) vector (CS1603B225), LgBiT-*CYBC1* (TK) vector,
636 (CS1603B226), *CYBC1*-LgBiT (TK) vector (CS1603B227), SmBiT-*CYBB* (TK) vector
637 (CS1603B228), *CYBB*-SmBiT (TK) vector (CS1603B229), LgBiT-*CYBB* (TK) vector
638 (CS1603B230), *CYBB*-LgBiT (TK) vector (CS1603B231). Promega also generated a LgBiT-
639 *CYBC1*-*CYBB*-SmBiT BiBiT vector (CS1603B292) and a LgBiT-*CYBC1* Bi-ready Vector
640 (CS1603B290) where fusions proteins are expressed from a single bi-directional CMV promoter.
641 NanoBiT Bi-Directional Vector Systems allow to control for transfection efficiency of separate
642 constructs. HEK293 were plated at a concentration of 2×10^4 cells per well in a 96 well plate (3917,
643 Corning). The following day, cells were transfected either with 55ng/well of the indicated vector
644 combinations (1:1 ratio of interacting pairs), the Bi-BiT ready Vectors or with the NanoBiT negative
645 and positive control provided (not shown in graphs), using EugeneHD reagent (E2311, Promega)
646 at a lipid to DNA ratio of 3:1. 20 hours post-transfection, growth-medium was exchanged with
647 OPTI-MEM (51985034, Thermo Fisher) containing 2% FBS (7534, Sigma Aldrich) and 20mM
648 HEPES (Thermo Fisher). The plate was left to equilibrate 10min at room temperature before
649 addition of the freshly reconstituted Nano-Glo Live cell substrate. Luminescence was subsequently
650 measured on a FLUOstar Omega plate reader (BMG, Labtech) using the following settings: plate
651 mode, number of cycles: 8; cycle interval: 900sec, gain adjustment 70% of the target (positive
652 control), orbital averaging of the well: 3; orbital shaking 300rpm for 15s before the first
653 measurement.

654 *Yeast 2 Hybrid experiment*

655 *gp91phox* and EROS analysis was performed by Hybrigenics Services (91000 Evry, France). The
656 coding sequences of human EROS/*CYBC1* (NM_001033046.3) and human *gp91phox*/*CYBB*
657 (NM_000397.3) were PCR-amplified and cloned in frame with the Gal4 DNA binding domain
658 (DBD) into plasmid pB66 (Fromont-Racine et al., 1997) as a C-terminal fusion to Gal4 (Gal4-DBD-
659 bait fusion) and with the Gal4 Activation Domain (AD) into plasmid pP7 (AD-prey fusion). The
660 diploid yeast cells were obtained using a mating protocol with both yeast strains (Fromont-Racine
661 et al., 1997), based on the HIS3 reporter gene (growth assay without histidine). As negative

662 controls, the bait plasmids were tested in the presence of empty prey vector and the prey plasmids
663 were tested with the empty bait vector. The interaction between SMAD and SMURF is used as
664 positive control (Colland et al., 2004). Controls and interactions were tested in the form of streaks
665 of three independent yeast clones for each control and interaction on DO-2 and DO-3 selective
666 media. The DO-2 selective medium lacking tryptophan and leucine was used as a growth control
667 and to verify the presence of the bait and prey plasmids. The DO-3 selective medium without
668 tryptophan, leucine, and histidine selects for the interaction between bait and prey. For specific
669 interactions, the selection pressure was increased using 0.5mM 3-Aminotriazol (3-AT). Yeast 2
670 Hybrid analysis of NOX family of proteins was performed as previously reported (Luck et al.,
671 2020).

672 *Cytokine secretion:*

673 For *in-vivo* experiments, EROS knockout mice were injected with 250ng/mL of LPS (Invivogen). 2h
674 later, 30mM of ATP or PBS (for control) was injected intraperitoneally. Mice were culled 2h later,
675 and the peritoneal cavity washed. Supernatants and serum were analysed for the presence of the
676 cytokines indicated in the figures using multiplex kits from Meso Scale Discovery (Maryland, US)
677 and were conducted at the Core Biochemical Assay Laboratory (Cambridge University Hospital,
678 UK).

679 *Caspase-1 activity measurement*

680 Peritoneal macrophages from control or EROS knockout mice were primed overnight with LPS
681 (100ng/mL, Invivogen) and treated for 2h with ATP (2.5mM, Invivogen). Supernatants were
682 harvested and subjected to Caspase-Glo 1 inflammasome assay following manufacturer's protocol
683 (G9951, Promega). Luminescence from caspase-1 activity was detected with a FLUOstar Omega
684 plate reader (BMG, Labtech).

685 *Immunofluorescence*

686 Cells expressing human pEGFP-N2-STT3A, human pmRFP-N2-EROS/C17ORF62 and human
687 pEGFP-N2-Lap2 β constructs (generously given by Prof. Eric Schirmer, University of Edinburgh,
688 UK) were fixed 15min in 4% paraformaldehyde (15710-S, Electron Microscopy), permeabilised

689 with 0.1% Triton X-100 (Sigma) and quenched in 100mM Glycine (Sigma) for 15min. To reduce
690 background, a blocking solution consisting of 5% Goat Serum (Sigma), 1% BSA (Sigma) in PBS
691 (Sigma) was applied for 1h prior to staining with the indicated primary antibody diluted in PBS
692 solution with 0.5% Goat Serum (Sigma), 0.5% BSA (Sigma) for 1h30 at room temperature.
693 Following extensive washes, cells were stained for 45min at room temperature with the
694 appropriate secondary antibodies from Life Technologies: goat anti-mouse IgG – Alexa 488
695 conjugated (A11029), goat anti-rabbit IgG -Alexa 555 conjugated (A21429) and/or goat anti-rabbit
696 IgG- Alexa 647 (A21245). Nucleus was labelled with Hoescht 33342 (H3570, Thermo Fisher)
697 before coverslips were mounted in Prolong Diamond (P36961, Life Technologies).
698 Images were acquired on a ZEISS LSM 780 system, equipped with the following lasers: diode
699 405nm, argon multiline 458/488/514nm, HeNe 543nm, HeNe 594nm and HeNe 633nm and using
700 a Plan Apochromat 63x/1.4 oil objective. Image processing and analysis of the intensity profile
701 were done on Fiji is just Image J software (version 1.53c) using the “plot profile” command.

702 *Calcium flux assay*

703 Calcium imaging was performed on EROS-deficient and control cells using the Rhod-3-AM
704 calcium imaging kit (Invitrogen) following the manufacturer's protocol. Images were acquired with
705 an LSM710 laser scanning META confocal microscope (Carl Zeiss) using a ×20 objective and
706 maximum pinhole aperture of 600µm. Two-line averages were performed for each frame with
707 images taken every 4s. 20µl of media was used as a negative control. At t = 140s, 100µM bzATP
708 was added to the cells. 100ng/ml ionomycin was used as a positive control at the end of the
709 experiment to confirm correct loading of cells. Image analysis of fluorescence intensity in response
710 to addition of negative control, bzATP and positive control across the time course was performed
711 with the Volocity 3D Image Analysis Software, collecting data for all cells that did not
712 spontaneously fluoresce and had an ionomycin response.

713 *Flow cytometry*

714 Single cell suspensions of spleens were prepared by mechanical disruption in FACS buffer (D-
715 PBS with 2mM EDTA, 0.5% FBS and 0.09% sodium azide) with a 100µm smart strainer (Miltenyi

716 Biotec). 10% of the spleen was subjected to red blood cell lysis (eBioscience), washed and
 717 blocked with 1µg of Mouse BD FC Block™ for 10min at 4°C prior to addition of multicolour
 718 antibody cocktails. After incubation for 30min DAPI was added (0.2µg/ml) and the samples
 719 washed prior to acquisition on a LSRFortessa™ (BD biosciences) that was standardised using BD
 720 Cytometer Setup and Tracking beads and software. Compensation was determined using
 721 Ultracomp eBeads (eBioscience). Data acquisition was controlled with BD FACSDiva v8 software.
 722 The antibody cocktails included anti-mouse antibodies from Miltenyi Biotec: CD44-FITC (clone
 723 IM7.8.1), CD62L-PerCP-Vio700 (clone REA828), CD25-PE-Vio770 (clone 7D4), NK1.1-APC
 724 (clone PK136), TCRγδ-Vioblue (clone GL3), CD4-Viogreen (clone GK1.5). Mouse anti-CD8α-APC-
 725 H7 (clone 53-6.7) and mouse TCRβ-BV711 (clone H57.597) were from BD Bioscience. Mouse
 726 anti-P2X7-PE (clone 1F11) and mouse anti-CD45-AF700 (clone 30-F11) were from Biolegend.
 727 All samples were analysed using FlowJo 10.7 in a blinded manner. Doublets were excluded via
 728 FSC-A vs FSC-H and SSC-H vs SSC-W and dead cells excluded by DAPI vs FSC-A. A plot of
 729 CD45 against time was used to check the stability of sample acquisition and leukocytes identified
 730 by a CD45 vs SSC-A plot. CD4 T cells are TCRβ+NK1.1-CD4+, CD8 T cells are TCRβ+NK1.1-
 731 CD8+, NK cells are TCRβ-NK1.1+, NKT cells are TCRβ+NK1.1+, γδT cells are TCRγδ+TCRβ- and
 732 B cells were TCRβ-NK1.1-TCRγδ-SSC low. A gate for P2X7 was set on each population based on
 733 a fluorescence minus one control.
 734 For shedding analysis, 100µl of CD4 cells were treated with either 29µM NAD (Sigma) or 2.5mM
 735 ATP (Invivogen) for 30mins at 37°C, washed, resuspended in FACS buffer (PBS, 2% FBS) and
 736 co-stained with anti-CD4 (GK1.5, Biolegend), anti-CD62L (MEL-14, Biolegend) and anti-CD27
 737 (LG.3A10, Biolegend) for 10min at room temperature. Unbound antibodies were removed by
 738 washing cells in FACS buffer and cells were kept in the same buffer for the acquisition.
 739 For cell death analysis, NAD or ATP-treated CD4 cells (as described above) were resuspended in
 740 annexin-binding buffer (Thermo Fisher) and incubated with 1µl 100µg/ml Propidium Iodide (PI;
 741 Thermo Fisher) and 1/50 annexin V antibody (Thermo Fisher) for 10min at room temperature.
 742 Cells were washed and resuspended in 1X annexin- binding buffer for the acquisition. Samples

743 were acquired on an LSR X20 flow cytometer (BD).

744 *EROS affinity purification-mass spectrometry*

745 EROS-FLAG affinity purifications were carried out as described previously (Thomas et al., 2017).

746 Bound proteins were eluted by incubating the beads with 200µg/ml 3xFLAG peptide (Sigma-

747 Aldrich) in IPP150 containing 0.02% NP-40. The eluates were concentrated in Vivaspin 500 PES

748 centrifugal filters (Vivascience), reduced with 5mM TCEP (Sigma-Aldrich), and alkylated with

749 10mM iodoacetamide prior to sample fractionation by polyacrylamide gel electrophoresis with

750 Novex NuPAGE Bis-Tris 4–12% gels (Life Technologies). Gels were stained with colloidal

751 Coomassie (Sigma) and whole gel lanes were excised into 12 bands and processed for mass

752 spectrometry analysis as previously described (Pardo et al., 2010).

753 Peptides were reconstituted in 0.1% formic acid and injected for on-line LC-MS/MS analysis on an

754 LTQ FT Ultra hybrid mass spectrometer coupled with an Ultimate 3000 RSLCnano UPLC system.

755 Peptides were separated on a PepMap C18 column (75µm i.d. x 250mm, 2µm) over a linear

756 gradient of 4 – 33.6% CH₃CN/0.1% formic acid in 60min at a flow rate at 300nl/min. MS analysis

757 used standard data-dependant acquisition mode to fragment the top 5 multiply charged ions with

758 intensity above 1000. Briefly, the FT full MS survey scan was m/z 380 – 1800 with resolution

759 100,000 at m/z 400, AGC set at 1e6 and 500ms maximum injection time. The MS/MS fragmented

760 in ion trap was set at 35% collision energy, with AGC at 1e4 and 250ms maximum injection time,

761 and isolation width at 2.0Da. The dynamic exclusion was set 45s with ± 20ppm exclusion window.

762 Raw files were processed with Proteome Discover 2.3 (Thermo Fisher Scientific). Database

763 searches were performed with Sequest HT against the mouse Uniprot database (v. August 2019)

764 and cRAP contaminant database. The search parameters were: trypsin, maximum of 2 missed

765 cleavages, 10ppm mass tolerance for MS, 0.5Da tolerance for MS/MS, with variable modifications

766 of carbamidomethyl (C), N-acetylation (protein N-term), deamidation (NQ), oxidation (M),

767 formylation (N-term) and Gln- > pyro-Glu (N-term Q). Database search results were refined

768 through processing with Percolator (FDR <1%). Protein identification required at least one high-

769 confidence peptide. External contaminants (keratins, albumin, casein, immunoglobulins) were

770 removed before further analysis. SAINTexpress was used to score interaction specificity (Teo et
771 al., 2014). Proteins with SAINT probability score > 0.9 were deemed high confidence specific
772 interactors (FDR< 1%). Proteins with SP score > 0.74 represent medium confidence interactors
773 (FDR < 5%).

774 For visualization, the protein interaction network was generated with STRING (minimum required
775 interaction score 0.4) using interactions derived from text-mining, experiments and databases. GO
776 term enrichment analysis was performed with STRING.

777 *Full proteome quantitative analysis by TMT-Mass spectrometry*

778 Cell pellets were lysed in 1% Sodium deoxyolate / 10% isopropanol / 50mM NaCl /100mM TEAB
779 (tetraethylammonium bromide, Sigma) with Halt™ Protease and Phosphatase Inhibitor Cocktail
780 (1x, Thermo Scientific). Lysates were sonicated and heated at 90°C for 5min. 100µg of proteins
781 per sample were reduced with TCEP, alkylated with iodoacetamide, and digested with 3µg of
782 trypsin (Pierce MS grade, Thermo) prior to labelling with TMT10plex according to the
783 manufacturer's instructions. Samples were pooled, acidified, and then centrifuged to remove
784 precipitated deoxycholic acid. The supernatant was dried, resuspended in 0.1% NH₄OH and
785 fractionated on an XBridge BEH C18 column (2.1mm i.d. x 150mm, Waters) with an initial 5min
786 loading then linear gradient from 5% CH₃CN/0.1% NH₄OH (pH 10) – 35% CH₃CN /0.1% NH₄OH
787 for 30min, then to 80% CH₃CN /0.1% NH₄OH for 5min and stayed for another 5min. The flow rate
788 was at 200µl/min. Fractions were collected at every 42s from 7.8min to 50min and then
789 concatenated to 28 fractions and dried.

790 Peptides were reconstituted in 0.1% formic acid and a 25% aliquot injected for on-line LC-MS/MS
791 analysis on the Orbitrap Fusion Lumos hybrid mass spectrometer coupled to an Ultimate 3000
792 RSLCnano UPLC system (Thermo Fisher). Samples were desalted on a PepMap C18 nano trap
793 (100µm i.d. x 20mm, 100 Å, 5µ), then separated on a PepMap C18 column (75µm i.d. x 500mm,
794 2µm) over a linear gradient of 5.6 – 30.4% CH₃CN/0.1% formic acid in 90min at a flow rate at
795 300nl/min. The MS acquisition used MS3 level quantification with Synchronous Precursor
796 Selection (SPS5) with the Top Speed 3s cycle time. Briefly, the Orbitrap full MS survey scan was

797 m/z 375 – 1500 with the resolution 120,000 at m/z 200, with AGC set at 4e5 and 50ms maximum
798 injection time. Multiply charged ions ($z = 2 - 5$) with intensity threshold at 5000 were fragmented in
799 ion trap at 35% collision energy, with AGC at 1e4 and 50ms maximum injection time, and isolation
800 width at 0.7Da in quadrupole. The top 5 MS2 fragment ions were SPS selected with the isolation
801 width at 0.7Da, fragmented in HCD at 65% NCE, and detected in the Orbitrap. The resolution was
802 set at 50,000, and the AGC at 1e5 with maximum injection time at 86ms. The dynamic exclusion
803 was set 40s with ± 10 ppm exclusion window.

804 Raw files were processed with Proteome Discoverer 2.4 (Thermo Fisher) using Sequest HT.
805 Spectra were searched against Uniprot mouse database (April 2020) and cRAP contaminant
806 database. Search parameters were: trypsin with 2 maximum miss-cleavage sites, mass tolerances
807 at 20ppm for precursors and 0.5Da for fragment ions, dynamic modifications of Deamidated (N,
808 Q), Oxidation (M) and Acetyl (Protein N-terminus), static modifications of Carbamidomethyl (C)
809 and TMT6plex (Peptide N-terminus and K). Peptides were validated by Percolator with q-value set
810 at 0.01 (strict) and 0.05 (relaxed). The TMT10plex reporter ion quantifier included 20ppm
811 integration tolerance on the most confident centroid peak at the MS3 level. The co-isolation
812 threshold was set at 100%. Only unique peptides, with average reported signal-to-noise ratio >3 ,
813 were used for protein quantification, and the SPS mass matches threshold was set at 55%. Only
814 master proteins were reported.

815 *Plasma Membrane Profiling analysis by Tandem Mass Tagging -Mass spectrometry*

816 Cell surface proteins were labelled essentially as described previously (Weekes et al., 2012).
817 Samples were then resuspended in 21 μ L 100mM TEAB pH 8.5 prior to labelling with Tandem
818 Mass Tagging (TMT) reagent (Thermo Fisher) following manufacturer's protocol. After checking
819 each sample was at least 98% TMT labelled, total reporter ion intensities were used to normalise
820 the pooling of the remaining samples to a 1:1 ratio of total peptide content between samples. This
821 final pool was brought up to a volume of 1mL with 0.1% TFA. FA was added until the pH was <2 .
822 Samples were then cleaned up by SPE using a 50mg tC18 SepPak cartridge (Waters). The
823 cartridge was wetted with 1mL 100% Methanol followed by 1mL ACN, equilibrated with 1mL 0.1%

824 TFA and sample loaded slowly. Samples were passed twice over the cartridge. The cartridge was
825 washed 3x with 1mL 0.1% TFA before eluting sequentially with 250µL 40% ACN, 70% ACN and
826 80% ACN and dried in a vacuum centrifuge.

827 TMT labelled samples were resuspended in 40µL 200mM Ammonium formate pH 10 and
828 transferred to a glass HPLC vial for basic pH reversed phase fractionation (BpH-RP). BpH-RP
829 fractionation was conducted on an Ultimate 3000 UHPLC system (Thermo Scientific) equipped
830 with a 2.1mm × 15cm, 1.7µm Kinetex EVO column (Phenomenex). Solvent A was 3% ACN,
831 Solvent B was 100% ACN, solvent C was 200mM ammonium formate (pH 10). Throughout the
832 analysis solvent C was kept at a constant 10%. The flow rate was 500 µL/min and UV was
833 monitored at 280nm. Samples were loaded in 90% A for 10min before a gradient elution of 0–10%
834 B over 10min (curve 3), 10-34% B over 21min (curve 5), 34-50% B over 5min (curve 5) followed
835 by a 10min wash with 90% B. 15s (100µL) fractions were collected throughout the run. Fractions
836 containing peptide (as determined by A280) were recombined across the gradient to preserve
837 orthogonality with on-line low pH RP separation. For example, fractions 1, 25, 49, 73, 97 were
838 combined and dried in a vacuum centrifuge and stored at -20°C until LC-MS analysis. 12 Fractions
839 were generated in this manner.

840 For mass spectrometry, analysis was conducted on an Orbitrap Fusion instrument on-line with an
841 Ultimate 3000 RSLCnano UHPLC system (Thermo Fisher). Samples were resuspended in 10µL
842 5% DMSO/1% TFA and all sample was injected. Trapping solvent was 0.1% TFA, analytical
843 solvent A was 0.1% FA, solvent B was ACN with 0.1% FA. Samples were loaded onto a trapping
844 column (300µm x 5mm PepMap cartridge trap (Thermo Fisher)) at 10µL/min for 5min at 60°C.
845 Samples were then separated on a 75cm x 75µm i.d. 2µm particle size PepMap C18 column
846 (Thermo Fisher) at 55°C. The gradient was 3-10% B over 10min, 10-35% B over 155min, 35-45%
847 B over 9min, followed by a wash at 95% B for 5min and re-equilibration at 3% B. Eluted peptides
848 were introduced by electrospray to the MS by applying 2.1kV to a stainless-steel emitter 5cm x
849 30µm (PepSep). Mass spectra were acquired using MS3 level quantification with SPS10 with the
850 Top Speed 3s cycle time. The Orbitrap full MS survey scan was m/z 400-1500 with the resolution

851 at 120 000, AGC set at 125 and 50ms maximum injection time. Multiple charged ions ($z=2-7$) with
852 intensity threshold at 5000 were fragmented in ion trap at 35% collision energy, with AGC at 80
853 and isolation width at 0.7Da in quadrupole. The top MS3 fragment ions were SPS selected with
854 the isolation width at 2 and were fragmented in HCD at 65% and detected in Orbitrap at 50 000
855 resolution. The AGC was set at 40 with maximum injection time at 120ms and the dynamic
856 exclusion was set at 40s with ± 10 ppm exclusion window.

857 Data were processed with MASCOT (Matrix Science) and Proteome discoverer, v2.2 (Thermo
858 Fisher). Raw files were searched against the UniProt Mouse database including common
859 contaminants at a MS1 Tol of 10ppm, MS2 Tol of 0.5Da. Fixed modifications were TMT labelled
860 Lysines and Peptide N-Termini and carbamidomethylated cysteines. Methionine oxidation was
861 allowed as a variable modification. Mascot Percolator was used to control the PSM FDR and an
862 automated decoy database search was used to determine protein FDR. Proteins with either “high”
863 (FDR <0.01) or “medium” (FDR <0.05) confidence were taken forward to further analysis. Proteins
864 and their abundances were output to .csv, imported to R and submitted to statistical analysis using
865 LIMMA, a moderated t-test available through the Bioconductor package. LIMMA p -values were
866 corrected for multiple hypothesis testing using the Benjamini-Hochberg method to generate an
867 FDR (q-value).

868 *Data availability*

869 The mass spectrometry proteomics data have been deposited to the ProteomeXchange
870 Consortium via the PRIDE (Perez-Riverol et al., 2019) partner repository with the dataset identifier
871 “PXD024659”. The plasma membrane profiling mass spectrometry data has the identifier
872 “PXD025149”.

873 **Acknowledgements**

874 D.C.T is funded by a Wellcome-Beit Prize Trust Clinical Research Career Development Fellowship
875 and the Burman Fund, Imperial College London. E.G and E.R.D. are funded by the Wellcome
876 Trust. This work was supported by the Italian Ministry of Education, University and Research
877 (MIUR, “Dipartimenti di Eccellenza Program 2018–2022—Dept. of Biology and Biotechnology L.
878 Spallanzani”, University of Pavia). We are grateful to Prof. Neil Bulleid for sharing the control,
879 *STT3A*^{-/-} and *STT3B*^{-/-} HEK293 originally from Prof. Reid Gilmore. We thank Prof. Arthur Kaser,
880 Prof. Eric Schirmer, Prof. Ramanujan Hedge, Prof. Marina Botto, Prof. Matthew Pickering and Dr.
881 Jacques Behmoaras for helpful discussion. We thank the Facility for Imaging by Light Microscopy
882 (FILM) at Imperial College London (London, UK), partly supported by funding from the Wellcome
883 Trust (grant 104931/Z/14/Z) and BBSRC (grant BB/L015129/1). We thank the LMS/NIHR Imperial
884 Biomedical Research Centre Flow Cytometry Facility for the support. We also thank the
885 Microscopy facility at the Cambridge Institute of Medical Research (Cambridge, UK).

886 **Competing interests**

887 The authors declare no competing interests.

- 889 ABO, A., PICK, E., HALL, A., TOTTY, N., TEAHAN, C. G. & SEGAL, A. W. 1991. Activation of the NADPH oxidase
890 involves the small GTP-binding protein p21rac1. *Nature*, 353, 668-70.
- 891 ALIMCHANDANI, M., LAI, J. P., AUNG, P. P., KHANGURA, S., KAMAL, N., GALLIN, J. I., HOLLAND, S. M.,
892 MALECH, H. L., HELLER, T., MIETTINEN, M. & QUEZADO, M. M. 2013. Gastrointestinal
893 histopathology in chronic granulomatous disease: a study of 87 patients. *Am J Surg Pathol*, 37,
894 1365-72.
- 895 ARNADOTTIR, G. A., NORDDAHL, G. L., GUDMUNDSDOTTIR, S., AGUSTSDOTTIR, A. B., SIGURDSSON, S.,
896 JENSSON, B. O., BJARNADOTTIR, K., THEODORS, F., BENONISDOTTIR, S., IVARSDOTTIR, E. V.,
897 ODDSSON, A., KRISTJANSSON, R. P., SULEM, G., ALEXANDERSSON, K. F., JULIUSDOTTIR, T.,
898 GUDMUNDSSON, K. R., SAEMUNDSDOTTIR, J., JONASDOTTIR, A., JONASDOTTIR, A., SIGURDSSON,
899 A., MANZANILLO, P., GUDJONSSON, S. A., THORISSON, G. A., MAGNUSSON, O. T., MASSON, G.,
900 ORVAR, K. B., HOLM, H., BJORNSSON, S., ARNGRIMSSON, R., GUDBJARTSSON, D. F.,
901 THORSTEINSDOTTIR, U., JONSDOTTIR, I., HARALDSSON, A., SULEM, P. & STEFANSSON, K. 2018. A
902 homozygous loss-of-function mutation leading to CYBC1 deficiency causes chronic granulomatous
903 disease. *Nat Commun*, 9, 4447.
- 904 BARTLETT, R., STOKES, L. & SLUYTER, R. 2014. The P2X7 receptor channel: recent developments and the
905 use of P2X7 antagonists in models of disease. *Pharmacol Rev*, 66, 638-75.
- 906 BEAUMEL, S., GRUNWALD, D., FIESCHI, F. & STASIA, M. J. 2014. Identification of NOX2 regions for normal
907 biosynthesis of cytochrome b558 in phagocytes highlighting essential residues for p22phox binding.
908 *Biochem J*, 464, 425-37.
- 909 BOUMECHACHE, M., MASIN, M., EDWARDSON, J. M., GORECKI, D. C. & MURRELL-LAGNADO, R. 2009.
910 Analysis of assembly and trafficking of native P2X4 and P2X7 receptor complexes in rodent immune
911 cells. *J Biol Chem*, 284, 13446-13454.
- 912 CECCON, M., MILLANA FANANAS, E., MASSARI, M., MATTEVI, A. & MAGNANI, F. 2017. Engineering stability
913 in NADPH oxidases: A common strategy for enzyme production. *Mol Membr Biol*, 34, 67-76.
- 914 CHEN, F., PANDEY, D., CHADLI, A., CATRAVAS, J. D., CHEN, T. & FULTON, D. J. 2011. Hsp90 regulates NADPH
915 oxidase activity and is necessary for superoxide but not hydrogen peroxide production. *Antioxid*
916 *Redox Signal*, 14, 2107-19.
- 917 CHEN, F., YU, Y., QIAN, J., WANG, Y., CHENG, B., DIMITROPOULOU, C., PATEL, V., CHADLI, A., RUDIC, R. D.,
918 STEPP, D. W., CATRAVAS, J. D. & FULTON, D. J. 2012. Opposing actions of heat shock protein 90 and
919 70 regulate nicotinamide adenine dinucleotide phosphate oxidase stability and reactive oxygen
920 species production. *Arterioscler Thromb Vasc Biol*, 32, 2989-99.
- 921 CHEREPANOVA, N., SHRIMAL, S. & GILMORE, R. 2016. N-linked glycosylation and homeostasis of the
922 endoplasmic reticulum. *Curr Opin Cell Biol*, 41, 57-65.
- 923 CHEREPANOVA, N. A. & GILMORE, R. 2016. Mammalian cells lacking either the cotranslational or
924 posttranslational oligosaccharyltransferase complex display substrate-dependent defects in
925 asparagine linked glycosylation. *Sci Rep*, 6, 20946.
- 926 CHOI, B. Y., KIM, J. H., KHO, A. R., KIM, I. Y., LEE, S. H., LEE, B. E., CHOI, E., SOHN, M., STEVENSON, M.,
927 CHUNG, T. N., KAUPPINEN, T. M. & SUH, S. W. 2015. Inhibition of NADPH oxidase activation reduces
928 EAE-induced white matter damage in mice. *J Neuroinflammation*, 12, 104.
- 929 COLLAND, F., JACQ, X., TROUPLIN, V., MOUGIN, C., GROIZELEAU, C., HAMBURGER, A., MEIL, A., WOJCIK, J.,
930 LEGRAIN, P. & GAUTHIER, J. M. 2004. Functional proteomics mapping of a human signaling
931 pathway. *Genome Res*, 14, 1324-32.
- 932 DE LUCA, A., SMEEKENS, S. P., CASAGRANDE, A., IANNITTI, R., CONWAY, K. L., GRESNIGT, M. S., BEGUN, J.,
933 PLANTINGA, T. S., JOOSTEN, L. A., VAN DER MEER, J. W., CHAMILOS, G., NETEA, M. G., XAVIER, R. J.,
934 DINARELLO, C. A., ROMANI, L. & VAN DE VEERDONK, F. L. 2014. IL-1 receptor blockade restores

autophagy and reduces inflammation in chronic granulomatous disease in mice and in humans. *Proc Natl Acad Sci U S A*, 111, 3526-31.

DE TORRE-MINGUELA, C., BARBERA-CREMADES, M., GOMEZ, A. I., MARTIN-SANCHEZ, F. & PELEGRIN, P. 2016. Macrophage activation and polarization modify P2X7 receptor secretome influencing the inflammatory process. *Sci Rep*, 6, 22586.

DELEO, F. R., BURRITT, J. B., YU, L., JESAITIS, A. J., DINAUER, M. C. & NAUSEEF, W. M. 2000. Processing and maturation of flavocytochrome b558 include incorporation of heme as a prerequisite for heterodimer assembly. *J Biol Chem*, 275, 13986-93.

DIEBOLD, B. A., WILDER, S. G., DE DEKEN, X., MEITZLER, J. L., DOROSHOW, J. H., MCCOY, J. W., ZHU, Y. & LAMBETH, J. D. 2019. Guidelines for the Detection of NADPH Oxidases by Immunoblot and RT-qPCR. *Methods Mol Biol*, 1982, 191-229.

DINAUER, M. C. 2019. Insights into the NOX NADPH Oxidases Using Heterologous Whole Cell Assays. *Methods Mol Biol*, 1982, 139-151.

DINAUER, M. C., PIERCE, E. A., BRUNS, G. A., CURNUTTE, J. T. & ORKIN, S. H. 1990. Human neutrophil cytochrome b light chain (p22-phox). Gene structure, chromosomal location, and mutations in cytochrome-negative autosomal recessive chronic granulomatous disease. *J Clin Invest*, 86, 1729-37.

DIXON, A. S., SCHWINN, M. K., HALL, M. P., ZIMMERMAN, K., OTTO, P., LUBBEN, T. H., BUTLER, B. L., BINKOWSKI, B. F., MACHLEIDT, T., KIRKLAND, T. A., WOOD, M. G., EGGERS, C. T., ENCELL, L. P. & WOOD, K. V. 2016. NanoLuc Complementation Reporter Optimized for Accurate Measurement of Protein Interactions in Cells. *ACS Chem Biol*, 11, 400-8.

FROMONT-RACINE, M., RAIN, J. C. & LEGRAIN, P. 1997. Toward a functional analysis of the yeast genome through exhaustive two-hybrid screens. *Nat Genet*, 16, 277-82.

GEMMER, M. & FORSTER, F. 2020. A clearer picture of the ER translocon complex. *J Cell Sci*, 133.

GOEHRING, A., LEE, C. H., WANG, K. H., MICHEL, J. C., CLAXTON, D. P., BACONGUIS, I., ALTHOFF, T., FISCHER, S., GARCIA, K. C. & GOUAUX, E. 2014. Screening and large-scale expression of membrane proteins in mammalian cells for structural studies. *Nat Protoc*, 9, 2574-85.

GOLDBLATT, D., BUTCHER, J., THRASHER, A. J. & RUSSELL-EGGITT, I. 1999. Chorioretinal lesions in patients and carriers of chronic granulomatous disease. *J Pediatr*, 134, 780-3.

HARPER, A. M., CHAPLIN, M. F. & SEGAL, A. W. 1985. Cytochrome b-245 from human neutrophils is a glycoprotein. *Biochem J*, 227, 783-8.

HARTUNG, H. P., SCHAFER, B., HEININGER, K. & TOYKA, K. V. 1988. Suppression of experimental autoimmune neuritis by the oxygen radical scavengers superoxide dismutase and catalase. *Ann Neurol*, 23, 453-60.

HENDRICKS, K. S., TO, E. E., LUONG, R., LIONG, F., ERLICH, J. R., SHAH, A. M., LIONG, S., O'LEARY, J. J., BROOKS, D. A., VLAHOS, R. & SELEMIDIS, S. 2022. Endothelial NOX4 Oxidase Negatively Regulates Inflammation and Improves Morbidity During Influenza A Virus Lung Infection in Mice. *Front Cell Infect Microbiol*, 12, 883448.

HOLMDAHL, R., SAREILA, O., OLSSON, L. M., BACKDAHL, L. & WING, K. 2016. Ncf1 polymorphism reveals oxidative regulation of autoimmune chronic inflammation. *Immunol Rev*, 269, 228-47.

HUET, G., RAJAKYLA, E. K., VIITA, T., SKARP, K. P., CRIVARO, M., DOPIE, J. & VARTIAINEN, M. K. 2013. Actin-regulated feedback loop based on Phactr4, PP1 and cofilin maintains the actin monomer pool. *J Cell Sci*, 126, 497-507.

JUMPER, J., EVANS, R., PRITZEL, A., GREEN, T., FIGURNOV, M., RONNEBERGER, O., TUNYASUVUNAKOOL, K., BATES, R., ZIDEK, A., POTAPENKO, A., BRIDGLAND, A., MEYER, C., KOHL, S. A. A., BALLARD, A. J., COWIE, A., ROMERA-PAREDES, B., NIKOLOV, S., JAIN, R., ADLER, J., BACK, T., PETERSEN, S., REIMAN, D., CLANCY, E., ZIELINSKI, M., STEINEGGER, M., PACHOLSKA, M., BERGHAMMER, T., BODENSTEIN, S., SILVER, D., VINYALS, O., SENIOR, A. W., KAVUKCUOGLU, K., KOHLI, P. & HASSABIS, D. 2021. Highly accurate protein structure prediction with AlphaFold. *Nature*, 596, 583-589.

KAWATE, T. & GOUAUX, E. 2006. Fluorescence-detection size-exclusion chromatography for precrystallization screening of integral membrane proteins. *Structure*, 14, 673-81.

986 KNAUS, U. G., HEYWORTH, P. G., EVANS, T., CURNUTTE, J. T. & BOKOCH, G. M. 1991. Regulation of
987 phagocyte oxygen radical production by the GTP-binding protein Rac 2. *Science*, 254, 1512-5.

988 KORFALI, N., WILKIE, G. S., SWANSON, S. K., SRSEN, V., BATRAKOU, D. G., FAIRLEY, E. A., MALIK, P.,
989 ZULEGER, N., GONCHAREVICH, A., DE LAS HERAS, J., KELLY, D. A., KERR, A. R., FLORENS, L. &
990 SCHIRMER, E. C. 2010. The leukocyte nuclear envelope proteome varies with cell activation and
991 contains novel transmembrane proteins that affect genome architecture. *Mol Cell Proteomics*, 9,
992 2571-85.

993 LEYVA-GRADO, V. H., ERMILER, M. E., SCHOTSAERT, M., GONZALEZ, M. G., GILLESPIE, V., LIM, J. K. &
994 GARCIA-SASTRE, A. 2017. Contribution of the Purinergic Receptor P2X7 to Development of Lung
995 Immunopathology during Influenza Virus Infection. *mBio*, 8.

996 LUCK, K., KIM, D. K., LAMBOURNE, L., SPIROHN, K., BEGG, B. E., BIAN, W., BRIGNALL, R., CAFARELLI, T.,
997 CAMPOS-LABORIE, F. J., CHARLOTEAUX, B., CHOI, D., COTE, A. G., DALEY, M., DEIMLING, S.,
998 DESBULEUX, A., DRICOT, A., GEBBIA, M., HARDY, M. F., KISHORE, N., KNAPP, J. J., KOVACS, I. A.,
999 LEMMENS, I., MEE, M. W., MELLOR, J. C., POLLIS, C., PONS, C., RICHARDSON, A. D., SCHLABACH, S.,
000 TEEKING, B., YADAV, A., BABOR, M., BALCHA, D., BASHA, O., BOWMAN-COLIN, C., CHIN, S. F., CHOI,
001 S. G., COLABELLA, C., COPPIN, G., D'AMATA, C., DE RIDDER, D., DE ROUCK, S., DURAN-FRIGOLA, M.,
002 ENNAJDAOUI, H., GOEBELS, F., GOEHRING, L., GOPAL, A., HADDAD, G., HATCHI, E., HELMY, M.,
003 JACOB, Y., KASSA, Y., LANDINI, S., LI, R., VAN LIESHOUT, N., MACWILLIAMS, A., MARKEY, D.,
004 PAULSON, J. N., RANGARAJAN, S., RASLA, J., RAYHAN, A., ROLLAND, T., SAN-MIGUEL, A., SHEN, Y.,
005 SHEYKHAKARIMLI, D., SHEYNKMAN, G. M., SIMONOVSKY, E., TASAN, M., TEJEDA, A., TROPEPE, V.,
006 TWIZERE, J. C., WANG, Y., WEATHERITT, R. J., WEILE, J., XIA, Y., YANG, X., YEGER-LOTEM, E., ZHONG,
007 Q., ALOY, P., BADER, G. D., DE LAS RIVAS, J., GAUDET, S., HAO, T., RAK, J., TAVERNIER, J., HILL, D. E.,
008 VIDAL, M., ROTH, F. P. & CALDERWOOD, M. A. 2020. A reference map of the human binary protein
009 interactome. *Nature*, 580, 402-408.

010 MAGNANI, A., BROSELIN, P., BEAUTE, J., DE VERGNES, N., MOUY, R., DEBRE, M., SUAREZ, F., HERMINE, O.,
011 LORTHOLARY, O., BLANCHE, S., FISCHER, A. & MAHLAOU, N. 2014. Inflammatory manifestations in
012 a single-center cohort of patients with chronic granulomatous disease. *J Allergy Clin Immunol*, 134,
013 655-662 e8.

014 MARTINEZ, J., CUNHA, L. D., PARK, S., YANG, M., LU, Q., ORCHARD, R., LI, Q. Z., YAN, M., JANKE, L., GUY, C.,
015 LINKERMANN, A., VIRGIN, H. W. & GREEN, D. R. 2016. Noncanonical autophagy inhibits the
016 autoinflammatory, lupus-like response to dying cells. *Nature*, 533, 115-9.

017 MARTINEZ, J., MALIREDDI, R. K., LU, Q., CUNHA, L. D., PELLETIER, S., GINGRAS, S., ORCHARD, R., GUAN, J.
018 L., TAN, H., PENG, J., KANNEGANTI, T. D., VIRGIN, H. W. & GREEN, D. R. 2015. Molecular
019 characterization of LC3-associated phagocytosis reveals distinct roles for Rubicon, NOX2 and
020 autophagy proteins. *Nat Cell Biol*, 17, 893-906.

021 MEISSNER, F., SEGER, R. A., MOSHOUS, D., FISCHER, A., REICHENBACH, J. & ZYCHLINSKY, A. 2010.
022 Inflammasome activation in NADPH oxidase defective mononuclear phagocytes from patients with
023 chronic granulomatous disease. *Blood*, 116, 1570-3.

024 NOUBADE, R., WONG, K., OTA, N., RUTZ, S., EIDENSCHENK, C., VALDEZ, P. A., DING, J., PENG, I., SEBRELL,
025 A., CAPLAZI, P., DEVOSS, J., SORIANO, R. H., SAI, T., LU, R., MODRUSAN, Z., HACKNEY, J. & OUYANG,
026 W. 2014. NRROS negatively regulates reactive oxygen species during host defence and
027 autoimmunity. *Nature*, 509, 235-9.

028 NUNOI, H., ROTROSEN, D., GALLIN, J. I. & MALECH, H. L. 1988. Two forms of autosomal chronic
029 granulomatous disease lack distinct neutrophil cytosol factors. *Science*, 242, 1298-301.

030 OLSSON, L. M., JOHANSSON, A. C., GULLSTRAND, B., JONSEN, A., SAEVARSDOTTIR, S., RONNBLOM, L.,
031 LEONARD, D., WETTERO, J., SJOWALL, C., SVENUNGSSON, E., GUNNARSSON, I., BENGTSSON, A. A. &
032 HOLMDAHL, R. 2017. A single nucleotide polymorphism in the NCF1 gene leading to reduced
033 oxidative burst is associated with systemic lupus erythematosus. *Ann Rheum Dis*, 76, 1607-1613.

034 PARDO, M., LANG, B., YU, L., PROSSER, H., BRADLEY, A., BABU, M. M. & CHOUDHARY, J. 2010. An expanded
035 Oct4 interaction network: implications for stem cell biology, development, and disease. *Cell Stem*
036 *Cell*, 6, 382-95.

037 PEREZ-RIVEROL, Y., CSORDAS, A., BAI, J., BERNAL-LLINARES, M., HEWAPATHIRANA, S., KUNDU, D. J.,
 038 INUGANTI, A., GRISS, J., MAYER, G., EISENACHER, M., PEREZ, E., USZKOREIT, J., PFEUFFER, J.,
 039 SACHSENBERG, T., YILMAZ, S., TIWARY, S., COX, J., AUDAIN, E., WALZER, M., JARNUCZAK, A. F.,
 040 TERNENT, T., BRAZMA, A. & VIZCAINO, J. A. 2019. The PRIDE database and related tools and
 041 resources in 2019: improving support for quantification data. *Nucleic Acids Res*, 47, D442-D450.
 042 PFEFFER, S., DUDEK, J., GOGALA, M., SCHORR, S., LINXWEILER, J., LANG, S., BECKER, T., BECKMANN, R.,
 043 ZIMMERMANN, R. & FORSTER, F. 2014. Structure of the mammalian oligosaccharyl-transferase
 044 complex in the native ER protein translocon. *Nat Commun*, 5, 3072.
 045 PFEIFFER, Z. A., GUERRA, A. N., HILL, L. M., GAVALA, M. L., PRABHU, U., AGA, M., HALL, D. J. & BERTICS, P. J.
 046 2007. Nucleotide receptor signaling in murine macrophages is linked to reactive oxygen species
 047 generation. *Free Radic Biol Med*, 42, 1506-16.
 048 PORTER, C. D., KURIBAYASHI, F., PARKAR, M. H., ROOS, D. & KINNON, C. 1996. Detection of gp91-phox
 049 precursor protein in B-cell lines from patients with X-linked chronic granulomatous disease as an
 050 indicator for mutations impairing cytochrome b558 biosynthesis. *Biochem J*, 315 (Pt 2), 571-5.
 051 PUSCHNIK, A. S., MARCEAU, C. D., OOI, Y. S., MAJZOU, K., RINIS, N., CONTESSA, J. N. & CARETTE, J. E.
 052 2017. A Small-Molecule Oligosaccharyltransferase Inhibitor with Pan-flaviviral Activity. *Cell Rep*, 21,
 053 3032-3039.
 054 RAMIREZ, A. S., KOWAL, J. & LOCHER, K. P. 2019. Cryo-electron microscopy structures of human
 055 oligosaccharyltransferase complexes OST-A and OST-B. *Science*, 366, 1372-1375.
 056 RINIS, N., GOLDEN, J. E., MARCEAU, C. D., CARETTE, J. E., VAN ZANDT, M. C., GILMORE, R. & CONTESSA, J.
 057 N. 2018. Editing N-Glycan Site Occupancy with Small-Molecule Oligosaccharyltransferase Inhibitors.
 058 *Cell Chem Biol*, 25, 1231-1241 e4.
 059 ROBINSON, L. E. & MURRELL-LAGNADO, R. D. 2013. The trafficking and targeting of P2X receptors. *Front*
 060 *Cell Neurosci*, 7, 233.
 061 ROSLI, S., KIRBY, F. J., LAWLOR, K. E., RAINCZUK, K., DRUMMOND, G. R., MANSELL, A. & TATE, M. D. 2019.
 062 Repurposing drugs targeting the P2X7 receptor to limit hyperinflammation and disease during
 063 influenza virus infection. *Br J Pharmacol*, 176, 3834-3844.
 064 RYODEN, Y., FUJII, T., SEGAWA, K. & NAGATA, S. 2020. Functional Expression of the P2X7 ATP Receptor
 065 Requires Eros. *J Immunol*, 204, 559-568.
 066 SALVATOR, H., MAHLAOU, N., CATHERINOT, E., RIVAUD, E., PILMIS, B., BORIE, R., CRESTANI, B.,
 067 TCHERAKIAN, C., SUAREZ, F., DUNOGUE, B., GOUGEROT-POCIDALO, M. A., HURTADO-NEDELEC, M.,
 068 DREYFUS, J. F., DURIEU, I., FOUYSSAC, F., HERMINE, O., LORTHOLARY, O., FISCHER, A. & COUDERC,
 069 L. J. 2015. Pulmonary manifestations in adult patients with chronic granulomatous disease. *Eur*
 070 *Respir J*, 45, 1613-23.
 071 SAREILA, O., HAGERT, C., KELKKA, T., LINJA, M., XU, B., KIHLEBERG, J. & HOLMDAHL, R. 2017. Reactive
 072 Oxygen Species Regulate Both Priming and Established Arthritis, but with Different Mechanisms.
 073 *Antioxid Redox Signal*, 27, 1473-1490.
 074 SCHEUPLEIN, F., SCHWARZ, N., ADRIOUCH, S., KREBS, C., BANNAS, P., RISSIEK, B., SEMAN, M., HAAG, F. &
 075 KOCH-NOLTE, F. 2009. NAD⁺ and ATP released from injured cells induce P2X7-dependent shedding
 076 of CD62L and externalization of phosphatidylserine by murine T cells. *J Immunol*, 182, 2898-908.
 077 SEGAL, A. W. 1987. Absence of both cytochrome b-245 subunits from neutrophils in X-linked chronic
 078 granulomatous disease. *Nature*, 326, 88-91.
 079 SEGAL, A. W. 2005. How neutrophils kill microbes. *Annu Rev Immunol*, 23, 197-223.
 080 SEGAL, A. W., HEYWORTH, P. G., COCKCROFT, S. & BARROWMAN, M. M. 1985. Stimulated neutrophils
 081 from patients with autosomal recessive chronic granulomatous disease fail to phosphorylate a Mr-
 082 44,000 protein. *Nature*, 316, 547-9.
 083 SELEMIDIS, S., SEOW, H. J., BROUGHTON, B. R., VINH, A., BOZINOVSKI, S., SOBEY, C. G., DRUMMOND, G. R.
 084 & VLAHOS, R. 2013. Nox1 oxidase suppresses influenza a virus-induced lung inflammation and
 085 oxidative stress. *PLoS One*, 8, e60792.
 086 SIM, J. A., PARK, C. K., OH, S. B., EVANS, R. J. & NORTH, R. A. 2007. P2X1 and P2X4 receptor currents in
 087 mouse macrophages. *Br J Pharmacol*, 152, 1283-90.

088 SNELGROVE, R. J., EDWARDS, L., RAE, A. J. & HUSSELL, T. 2006. An absence of reactive oxygen species
089 improves the resolution of lung influenza infection. *Eur J Immunol*, 36, 1364-73.

090 SOLIMINI, N. L., LIANG, A. C., XU, C., PAVLOVA, N. N., XU, Q., DAVOLI, T., LI, M. Z., WONG, K. K. & ELLEDGE,
091 S. J. 2013. STOP gene Phactr4 is a tumor suppressor. *Proc Natl Acad Sci U S A*, 110, E407-14.

092 STARK, R., WESSELINK, T. H., BEHR, F. M., KRAGTEN, N. A. M., ARENS, R., KOCH-NOLTE, F., VAN GISBERGEN,
093 K. & VAN LIER, R. A. W. 2018. T RM maintenance is regulated by tissue damage via P2RX7. *Sci*
094 *Immunol*, 3.

095 SUN, Z. & FASSLER, R. 2012. A firm grip does not always pay off: a new Phact(r) 4 integrin signaling. *Genes*
096 *Dev*, 26, 1-5.

097 TEO, G., LIU, G., ZHANG, J., NESVIZHSKII, A. I., GINGRAS, A. C. & CHOI, H. 2014. SAINTexpress:
098 improvements and additional features in Significance Analysis of INTERactome software. *J*
099 *Proteomics*, 100, 37-43.

100 THOMAS, D. C. 2017. The phagocyte respiratory burst: Historical perspectives and recent advances.
101 *Immunol Lett*, 192, 88-96.

102 THOMAS, D. C. 2018. How the phagocyte NADPH oxidase regulates innate immunity. *Free Radic Biol Med*,
103 125, 44-52.

104 THOMAS, D. C., CHARBONNIER, L. M., SCHEJTMAN, A., ALDHEKRI, H., COOMBER, E. L., DUFFICY, E. R.,
105 BEENKEN, A. E., LEE, J. C., CLARE, S., SPEAK, A. O., THRASHER, A. J., SANTILLI, G., AL-MOUSA, H.,
106 ALKURAYA, F. S., CHATILA, T. A. & SMITH, K. G. C. 2018. EROS/CYBC1 mutations: Decreased NADPH
107 oxidase function and chronic granulomatous disease. *J Allergy Clin Immunol*, 143, 782-785 e1.

108 THOMAS, D. C., CLARE, S., SOWERBY, J. M., PARDO, M., JUSS, J. K., GOULDING, D. A., VAN DER WEYDEN, L.,
109 STORISTEANU, D., PRAKASH, A., ESPELI, M., FLINT, S., LEE, J. C., HOENDERDOS, K., KANE, L.,
110 HARCOURT, K., MUKHOPADHYAY, S., UMRANIA, Y., ANTROBUS, R., NATHAN, J. A., ADAMS, D. J.,
111 BATEMAN, A., CHOUDHARY, J. S., LYONS, P. A., CONDLIFFE, A. M., CHILVERS, E. R., DOUGAN, G. &
112 SMITH, K. G. 2017. Eros is a novel transmembrane protein that controls the phagocyte respiratory
113 burst and is essential for innate immunity. *J Exp Med*, 214, 1111-1128.

114 TO, E. E., LUONG, R., DIAO, J., JJ, O. L., BROOKS, D. A., VLAHOS, R. & SELEMIDIS, S. 2019. Novel endosomal
115 NOX2 oxidase inhibitor ameliorates pandemic influenza A virus-induced lung inflammation in mice.
116 *Respirology*, 24, 1011-1017.

117 TO, E. E., VLAHOS, R., LUONG, R., HALLS, M. L., READING, P. C., KING, P. T., CHAN, C., DRUMMOND, G. R.,
118 SOBEY, C. G., BROUGHTON, B. R. S., STARKEY, M. R., VAN DER SLUIS, R., LEWIN, S. R., BOZINOVSKI,
119 S., O'NEILL, L. A. J., QUACH, T., PORTER, C. J. H., BROOKS, D. A., O'LEARY, J. J. & SELEMIDIS, S. 2017.
120 Endosomal NOX2 oxidase exacerbates virus pathogenicity and is a target for antiviral therapy. *Nat*
121 *Commun*, 8, 69.

122 TOM, R., BISSON, L. & DUROCHER, Y. 2008. Transfection of HEK293-EBNA1 Cells in Suspension with Linear
123 PEI for Production of Recombinant Proteins. *CSH Protoc*, 2008, pdb prot4977.

124 TREMBLAY-LAGANIERE, C., KAIYRZHANOV, R., MAROOFIAN, R., NGUYEN, T. T. M., SALAYEV, K., CHILTON, I.
125 T., CHUNG, W. K., MADDEN, J. A., PHORNPHUTKUL, C., AGRAWAL, P. B., HOULDEN, H. & CAMPEAU,
126 P. M. 2021. PIGH deficiency can be associated with severe neurodevelopmental and skeletal
127 manifestations. *Clin Genet*, 99, 313-317.

128 TUNYASUVUNAKOOL, K., ADLER, J., WU, Z., GREEN, T., ZIELINSKI, M., ZIDEK, A., BRIDGLAND, A., COWIE, A.,
129 MEYER, C., LAYDON, A., VELANKAR, S., KLEYWEGT, G. J., BATEMAN, A., EVANS, R., PRITZEL, A.,
130 FIGURNOV, M., RONNEBERGER, O., BATES, R., KOHL, S. A. A., POTAPENKO, A., BALLARD, A. J.,
131 ROMERA-PAREDES, B., NIKOLOV, S., JAIN, R., CLANCY, E., REIMAN, D., PETERSEN, S., SENIOR, A. W.,
132 KAVUKCUOGLU, K., BIRNEY, E., KOHLI, P., JUMPER, J. & HASSABIS, D. 2021. Highly accurate protein
133 structure prediction for the human proteome. *Nature*, 596, 590-596.

134 VAN WILGENBURG, B., BROWNE, C., VOWLES, J. & COWLEY, S. A. 2013. Efficient, long term production of
135 monocyte-derived macrophages from human pluripotent stem cells under partly-defined and fully-
136 defined conditions. *PLoS One*, 8, e71098.

137 VOLPP, B. D., NAUSEEF, W. M. & CLARK, R. A. 1988. Two cytosolic neutrophil oxidase components absent
138 in autosomal chronic granulomatous disease. *Science*, 242, 1295-7.

139 WALLACH, T. M. & SEGAL, A. W. 1997. Analysis of glycosylation sites on gp91phox, the flavocytochrome of
140 the NADPH oxidase, by site-directed mutagenesis and translation in vitro. *Biochem J*, 321 (Pt 3),
141 583-5.

142 WEEKES, M. P., ANTROBUS, R., TALBOT, S., HOR, S., SIMECEK, N., SMITH, D. L., BLOOR, S., RANDOW, F. &
143 LEHNER, P. J. 2012. Proteomic plasma membrane profiling reveals an essential role for gp96 in the
144 cell surface expression of LDLR family members, including the LDL receptor and LRP6. *J Proteome*
145 *Res*, 11, 1475-84.

146 WEGNER, J., ZILLINGER, T., SCHLEE-GUIMARAES, T. M., BARTOK, E. & SCHLEE, M. 2021. An epigenetic GPI
147 anchor defect impairs TLR4 signaling in the B cell transdifferentiation model for primary human
148 monocytes BLaER1. *Sci Rep*, 11, 14983.

149 WIENTJES, F. B., HSUAN, J. J., TOTTY, N. F. & SEGAL, A. W. 1993. p40phox, a third cytosolic component of
150 the activation complex of the NADPH oxidase to contain src homology 3 domains. *Biochem J*, 296 (Pt 3),
151 557-61.

152 YEUNG, A. T. Y., HALE, C., LEE, A. H., GILL, E. E., BUSHELL, W., PARRY-SMITH, D., GOULDING, D., PICKARD,
153 D., ROUMELIOTIS, T., CHOUDHARY, J., THOMSON, N., SKARNES, W. C., DOUGAN, G. & HANCOCK, R.
154 E. W. 2017. Exploiting induced pluripotent stem cell-derived macrophages to unravel host factors
155 influencing Chlamydia trachomatis pathogenesis. *Nat Commun*, 8, 15013.

156 YU, L., DELEO, F. R., BIBERSTINE-KINKADE, K. J., RENEE, J., NAUSEEF, W. M. & DINAUER, M. C. 1999.
157 Biosynthesis of flavocytochrome b558 . gp91(phox) is synthesized as a 65-kDa precursor (p65) in
158 the endoplasmic reticulum. *J Biol Chem*, 274, 4364-9.

159 YU, L., ZHEN, L. & DINAUER, M. C. 1997. Biosynthesis of the phagocyte NADPH oxidase cytochrome b558.
160 Role of heme incorporation and heterodimer formation in maturation and stability of gp91phox
161 and p22phox subunits. *J Biol Chem*, 272, 27288-94.

162 ZHONG, J., OLSSON, L. M., URBONAVICIUTE, V., YANG, M., BACKDAHL, L. & HOLMDAHL, R. 2018.
163 Association of NOX2 subunits genetic variants with autoimmune diseases. *Free Radic Biol Med*, 125,
164 72-80.

Figure Legends

Figure 1: EROS stabilises the expression of gp91 phox precursor. (A-C) Mouse constructs encoding EROS and gp91 phox were co-transfected into NIH3T3 **(A)**, COS-7 **(B)** and HEK293T **(C)** cell lines. gp91 phox expression was analysed by immunoblotting; arrow indicates gp91 phox band; ns: non-specific band. **(D-F)** gp91 phox and p22 phox expression in HEK293T cells following transfection with the indicated human constructs. **(G)** Left panel: Analysis of the stability of the different forms of gp91 phox (indicated by the arrows) following transfection in HEK293T cells in presence or absence of EROS and treatment with 10 $\mu\text{g/mL}$ cycloheximide. Right panel: Quantitation of the cycloheximide assay (mean of 4 independent experiments; error bars indicate SD) represented as a fold change of gp91 phox in cells expressing gp91 phox and EROS vectors relative to gp91 phox vector alone at 0h and normalized to actin expression. Actin and vinculin were used as loading control. **(H)** Stability of endogenous gp91 phox in PLB985 neutrophil-like cells overexpressing lentivirus (LV) EROS-GFP vector (MW \approx 41kDa) and treated with 10 $\mu\text{g/mL}$ cycloheximide. **(I-J)** gp91 phox expression following lentiviral transduction of EROS-GFP, gp91 phox or both in differentiated PL985 knockout (KO) for p22 phox **(I)** or EROS **(J)**. Data are representative of 3 independent experiments. See also Figure 1- figure supplement 1 and Figure 1- Source Data 1-4.

Figure 2: EROS regulates flavocytochrome b formation via direct binding to gp91 phox . (A-D) Immunoprecipitation (IP) and size exclusion chromatography (SEC) analysis of protein complexes associated with EROS. **(A)** IP of EROS in HEK293-F cells expressing StreptII-FLAG-tagged EROS, gp91 phox -GFP and p22 phox with western blot for gp91 phox . Lysates treated with Peptide N-glycosidase F (PNGaseF) or Endoglycosidase H (EndoH) served as reference; FG: fully glycosylated; PG: partially glycosylated; NG: non-glycosylated; Tot: total lysate; RT: run through; Elu: eluate. **(B)** SEC profile of EROS-IP eluate indicating protein (280nm) and heme (414nm) content. **(C)** Immunoblot analysis of gp91 phox -GFP, EROS-FLAG and endogenous p22 phox in SEC fraction 9-14 and 15-18. **(D)** SEC profile of EROS eluate from HEK293-F cells expressing

191 EROS-FLAG, gp91*phox* and p22*phox* constructs and treated with heme biosynthesis inhibitor
 192 succinyl acetone (10µg/ml). **(E)** IP of StrepII-FLAG-tagged EROS in HEK293-F treated with
 193 succinyl acetone. **(F)** Interaction between gp91*phox* and EROS assessed through luminescence
 194 production in live HEK293T cells expressing the indicated plasmids fused with the large (LgBIT) or
 195 small (SmBIT) fragment of the NanoLuc luciferase (see methods). Halo Tag (HT)-SmBIT is the
 196 negative control; RLU: Relative Luminescence Unit. **(G)** Yeast growth phenotypes obtained with
 197 the specified selective media using gp91*phox* bait plasmid and EROS prey plasmid. L: leucine; W:
 198 tryptophan; H: histidine; DBD: DNA binding domain of Gal4; AD: Activation domain of Gal4 (see
 199 methods). **(H)** EROS localisation in HEK293 cells transfected with EROS construct (top panel; 3D
 200 stack) or EROS and Lap2-GFP constructs (bottom panel; single plane), fixed, permeabilised and
 201 labelled with anti-EROS and anti-calnexin antibodies. Scale bar= 5µm. Data are representative of
 202 at least 3 independent experiments; error bars indicate SEM of triplicates. See also Figure 2-
 203 figure supplement 1. Figure 2- Source Data 1-2.

204 **Figure 3: EROS interacts and colocalises with the OST complex.** **(A)** EROS-FLAG affinity
 205 purification-mass spectrometry (AP-MS). Graph showing abundance (average number of peptide
 206 spectrum matches across 4 biological replicates) of all proteins identified in the FLAG AP-MS
 207 experiments (blue and red dots) versus their interactor specificity (SAINT probability score: SP).
 208 The red line marks the SP score cut-off (0.9) for high confidence interacting proteins. Proteins
 209 (dots) above this cut-off (59) are deemed high-confidence interactors. The bait (EROS) and
 210 interacting proteins relevant to this study are shown in red. **(B)** Protein interaction network of the
 211 59 high confidence EROS-interacting proteins (SP>0.9). The protein interactions were derived
 212 from STRING. Coloured nodes represent proteins annotated with enriched GO terms relevant to
 213 this study. **(C-D)** EROS and gp91*phox* localisation, following fixation and labelling with anti-EROS
 214 antibody, in HEK293 cells expressing STT3A-GFP and EROS constructs **(C)** or STT3A-GFP,
 215 gp91*phox*-mRFP and EROS untagged constructs **(D)**; scale bars= 5µm. Graphs represent the
 216 intensity profile of STT3A-GFP and EROS signal or STT3A-GFP, gp91*phox*-mRFP and EROS

217 signal measured across the nuclear membrane (indicated in red line). **(E)** Expression of *gp91^{phox}*
218 in HEK293 cells transfected with the indicated constructs and treated with OST inhibitor (NGI-1) at
219 the indicated concentration. **(F)** Expression of *gp91^{phox}* in control and *STT3A^{-/-}* or *STT3B^{-/-}*
220 HEK293 cells transfected with the indicated vectors. **(G)** Expression of *gp91^{phox}* in PLB985 cell
221 line treated with NGI-1 at the indicated concentration. Data are representative of 3 independent
222 experiments. See also Figure 3- figure supplement 1, Figure 3 – Source Data 1-3.

223 **Figure 4: Mass spectrometry analysis of proteins modulated by EROS in immune cells**
224 **identified the P2X7 purinergic receptor. (A)** Cartoon representation of the AlphaFold structure
225 prediction of the top ranked model. The structure is coloured according to the model quality with
226 dark blue representing residues with a predicted local Distance Difference Test (pLDDT) score
227 greater than 90, light blue pLDDT>70, yellow pLDDT>50 and red pLDDT ≤50. **(B-D)** Volcano plot of
228 proteins detected by Tandem Mass Tagging proteomics analysis of bone marrow derived
229 macrophages: BMDM **(B)** and CD4⁺ T lymphocytes **(C)** isolated from control and EROS knockout
230 (KO) mice. **(D)** Volcano plot of proteins recovered by Plasma Membrane Profiling of macrophages
231 isolated from control and EROS knockout (KO) mice. The volcano plots display statistical
232 significance (-log₁₀ p-value) versus the log₂ fold change from 5 biological replicates.

233 **Figure 5: EROS regulates P2X7 protein abundance by direct interaction and independently**
234 **of the NADPH oxidase. (A-D)** P2X7 expression analysed by western blotting of macrophages
235 isolated from control, EROS knockout (KO) **(A)** and *gp91^{phox}* knockout (KO) mice **(B)**, iPS-
236 derived macrophages control or EROS-deficient **(C)** and of control PLB985 cells and an EROS-
237 deficient clone **(D)**. **(E-F)** P2X7 expression in RAW264.7 cells overexpressing a FLAG- tagged
238 EROS vector **(E)** and in HEK293 cells transiently expressing the specified constructs **(F)**. **(G-H)**
239 Interaction between EROS and P2X7 probed by immunoprecipitation (IP) of EROS from
240 RAW264.7 EROS-FLAG macrophages followed by immunoblot (IB) for P2X7 **(G)** and by NanoBIT
241 assay in live HEK293 cells expressing the LgBIT-fused EROS vector with a SmBIT-fused P2X7

242 vector **(H)**. **(I)** P2X1 expression in macrophages isolated from EROS knockout (KO) mice
243 compared to control. n= 5 biological replicates. **(J)** P2X1 abundance upon co-transfection with
244 EROS construct in HEK293 cells. Data are representative of 3 independent experiments; error
245 bars indicate SEM of triplicates. See also Figure 5- figure supplement 1 and Figure 5- Source Data
246 1-4.

247 **Figure 6: Functional consequences of low P2X7 expression in EROS-deficient cells. (A)**
248 Calcium release tested by Rhod-3-AM calcium imaging assay, in control or EROS-deficient BMDM
249 in response to bzATP treatment (with ionomycin as positive control); data is representative of 3
250 independent experiments. **(B)** IL-1 β secretion following LPS priming of peritoneal macrophages
251 from control or EROS knockout (KO) mice before and after treatment with ATP. **(C)** Secretion of
252 IL-1 β following *in vivo* administration of LPS and then ATP to control or EROS knockout (KO) mice
253 (n=3-5 biological replicates). **(D)** Decreased Caspase-1 activity, detected through luminescence
254 production (see methods), in peritoneal macrophages from EROS knockout (KO) mice compared
255 to control mice following LPS priming and ATP treatment (n= 11 biological replicates). **(E-F)**
256 Representative flow cytometry histogram of surface ligand CD62L **(E)** and CD27 **(F)** expression in
257 CD4⁺ T cells isolated from EROS knockout (KO) or control mice and treated with ATP (n= 5
258 biological replicates). Percentage of CD4⁺ T cells positive for CD62L or CD27 for each condition is
259 shown on the left panel graphs. **(G)** Reduced phosphatidyl serine exposure and cell death in
260 EROS-deficient CD4⁺ T cells compared to control CD4⁺ T cells following ATP treatment as
261 analysed by flow cytometry staining with Propidium Iodide and Annexin V. Left panel graph shows
262 the percentage of CD4⁺ T cells undergoing apoptosis in each condition (representative of n= 5
263 biological replicates). **(H)** Control or EROS knockout (KO) mice were infected intranasally with
264 3.10³ PFU of A/X31 influenza. Signs of illness were monitored daily (n= 17 control, 15 EROS
265 knockout biological replicates). *p* value was determined using unpaired Student's *t* test; error bars
266 indicate SEM. See also Figure 6- figure supplement 1.

267 **Figure Supplement Legend**

268 **Figure 1 - figure supplement 1: EROS specifically regulates gp91 phox not p22 phox**
269 **expression. (A)** Expression of gp91 phox in human iPS-derived macrophage deficient for EROS
270 (lanes are triplicate). **(B)** Diagram depicting the different stages of gp91 phox biosynthesis and
271 formation of the heterodimer with p22 phox . **(C)** gp91 phox expression upon co-expression of
272 gp91 phox -GFP and EROS-FLAG vectors compared to gp91 phox GFP alone in non-adherent
273 HEK293-F. **(D)** Abundance of the 58kDa form of gp91 phox in mouse NIH3T3 cells upon co-
274 expression of gp91 phox and EROS human constructs. **(E)** Expression of p22 phox in HEK293 cells
275 co-transfected with p22 phox and EROS mouse constructs compared to p22 phox vector alone
276 (lanes are triplicate). **(F)** Expression level of EROS in bone marrow derived macrophages (BMDM)
277 from gp91 phox knockout (KO) mice compared to control mice. Data are representative of 3
278 independent experiments. **(G)** Histogram derived from gp91 phox stability curve (Figure 1H) in
279 absence (blue) or presence (red) of EROS (4 independent experiments; p value was determined
280 using unpaired Student's t test; error bars indicate SD). See also Figure 1- figure supplement 1
281 Source Data 1-3.

282 **Figure 2 - figure supplement 1: EROS acts at the early stage of gp91 phox biosynthesis. (A)**
283 Interaction of endogenous gp91 phox and EROS analyzed by immunoprecipitation (IP) of
284 gp91 phox followed by immunoblot of EROS in PLB985 cells. Immunoblot with p22 phox serves as
285 positive control (dashed lines indicate different exposure time). **(B)** Luminescence production from
286 the 8 different combinations of gp91 phox (CYBB) and EROS (CYBC1) tagged with the Large (L:
287 LgBiT) fragment or Small (S: SmBiT) fragment of the luciferase compared to combination with the
288 Halo-Tag SmBiT (HT-S) control vector in HEK293 cells. Red box indicates selected constructs
289 pair. **(C)** NanoBiT assay in HEK293 cells using gp91 phox (CYBB) and EROS (CYBC1) encoded in
290 a single construct (L-CYBC1-CYBB-S; see method); L-CYBC1 co-transfected with HT-S is the
291 negative control. **(D)** HEK293 transfected with the indicated constructs were treated (right panel)
292 or not (left panel) with succinyl acetone prior to analysis of NOX2 (gp91 phox) expression. **(E-G)**

293 Effect of EROS on the abundance of NOX2 homologues NOX1 **(E)**, NOX4 **(F)** and NOX5 **(G)** in
294 HEK293 or HEK293-F transfected with the indicated tagged constructs and treated or not with
295 succinyl acetone (10µg/mL). **(H)** Yeast 2 Hybrid analysis of EROS direct binding to NOX proteins
296 family. **(I)** Expression of *nox1* and *nox4* in the specified tissues taken from control and EROS
297 knockout (KO) mice (n=4 biological replicates). Data are representative of 3 independent
298 experiments; error bars indicate SEM of triplicates. See also Figure 2- figure supplement 1 Source
299 Data 1-5.

300 **Figure 2 - figure supplement 2:** Diagram depicting the role of EROS in gp91*phox* biosynthesis
301 and formation of the heterodimer with p22*phox*.

302 **Figure 3 - figure supplement 1:** **(A)** gp91*phox* expression in control, *STT3A*^{-/-}, *STT3B*^{-/-} HEK293
303 transfected with the indicated constructs and treated with 10µM NGI-1 or 2µg/mL tunicamycin. **(B)**
304 Expression level of the ER-stress marker BiP in control and *STT3A*^{-/-} or *STT3B*^{-/-} HEK293 cells
305 transfected with the indicated constructs. **(C)** Immunoblot control of STT3A expression in control
306 and *STT3A*^{-/-} or *STT3B*^{-/-} HEK293 cells; Exp: experiment. **(D)** Expression level of BiP upon
307 treatment of PLB985 cells with different concentrations of the glycosylation inhibitors NGI-1 or
308 tunicamycin. Data are representative of at least 2 independent experiments. See also Figure 3-
309 figure supplement 1 Source Data 1-2.

310 **Figure 5 - figure supplement 1: P2X7 expression is lower in numerous cell subsets**
311 **from EROS knockout mice.** **(A)** P2X7 measured by surface flow cytometry staining of bone
312 marrow derived macrophages (BMDM) from control and EROS knockout (KO) mice. **(B)**
313 P2X7 level in peritoneal macrophages from control and EROS knockout (KO) mice
314 expressed by mean fluorescence intensity (left panel) and percentage of positive cells (right
315 panel). **(C)** Western blot of P2X7, EROS and actin expression in control and EROS-deficient
316 whole splenic CD4 T cells. **(D-I)** Percentage of cells that are P2X7 positive in the specified

317 splenic cell subsets. **(J)** Expression of P2X7 in HEK293 cells measured by flow cytometry
318 following co-transfection with EROS. **(K)** Expression of the P2X7 homologue P2X4 in control
319 and EROS-deficient BMDM analyzed by western blotting with the indicated antibody. n= 3-5
320 biological replicates. *p* value was determined using Student's t test; error bars indicate SEM.
321 See also Figure 5- figure supplement 1 Source Data 1-2.

322 **Figure 6- figure supplement 1: Cytokine profile and surface ligand expression in**
323 **EROS-deficient cell subsets. (A-B)** *In vitro* secretion of the indicated cytokines pre- and
324 post-ATP treatment of control and EROS-deficient peritoneal macrophages (n= 3 biological
325 replicates). **(C-F)** *In vivo* secretion of the indicated cytokines in control and EROS knockout
326 (KO) mice following ATP injection (n=3-5 biological replicates). **(G-H)** Representative flow
327 cytometry histogram of surface ligand CD62L **(G)** and CD27 **(H)** expression in CD4 T cells
328 isolated from EROS knockout (KO) or control mice and treated with NAD. Percentage of CD4
329 T cells positive for CD62L or CD27 for each condition is shown on the left panel graphs (n=5
330 biological replicates). *p* value was determined using Student's t test; error bars indicate SEM.

331 **Supplementary File 1: Primers used to generate iPS cells knockout for EROS by**
332 **CRISPR (A)** Sequences of the CRISPR guide RNA and the gene specific genotyping primers
333 (GF1-GR1) **(B)** Validation of EROS knockout (gene CYBC1) by Sanger sequencing.

334 **Source data files**

335 Figure 1- Source Data 1: Raw unedited blots for Figure 1A-C

336 Figure 1- Source Data 2: Raw unedited blots for Figure 1D-F

337 Figure 1- Source Data 3: Raw unedited blots for Figure 1G-J

338 Figure 1- Source Data 4: Uncropped gels used for Figure 1A-J

339 Figure 1- figure supplement 1- Source Data 1: Raw unedited blots for Figure 1- figure
340 supplement 1A, 1C, 1D

341 Figure 1- figure supplement 1- Source Data 2: Raw unedited blots for Figure 1- figure
342 supplement 1E-F

343 Figure 1- figure supplement 1- Source Data 3: Uncropped gels used for Figure 1A, 1C, 1D,
344 1E, 1F

345 Figure 2- Source data 1: Raw unedited blots for Figure 2A, 2C, 2E

346 Figure 2- Source data 2: Uncropped gels used for Figure 2

347 Figure 2- figure supplement 1- Source Data 1: Raw unedited blots for Figure 2- figure
348 supplement 1A, 1D

349 Figure 2- figure supplement 1- Source Data 2: Raw unedited blots for Figure 2- figure
350 supplement 1E, 1F, 1G

351 Figure 2- figure supplement 1- Source Data 3: Raw unedited blots for Figure 2- figure
352 supplement 1I

353 Figure 2- figure supplement 1- Source Data 4: Uncropped gels used for Figure 2- figure
354 supplement 1A, 1D, 1E, 1F

355 Figure 2- figure supplement 1- Source Data 5: Uncropped gels used for Figure 2- figure
356 supplement 1G-I

357 Figure 3- Source Data 1: Table of the 59 proteins identified in EROS IP-MS interactome

358 Figure 3- Source Data 2: Raw unedited blots for Figure 3E-G

359 Figure 3- Source Data 3: Uncropped gels used for Figure 3E-G

360 Figure 3- figure supplement 1- Source Data 1: Raw unedited blots for Figure 3- figure

361 supplement 1A-D

362 Figure 3- figure supplement 1- Source Data 2: Uncropped blots for Figure 3- figure
363 supplement 1A-D

364 Figure 5- Source Data 1: Raw unedited blots for Figure 5A-D

365 Figure 5- Source Data 2: Raw unedited blots for Figure 5E-G

366 Figure 5- Source Data 3: Raw unedited blots for Figure 5I-J

367 Figure 5- Source Data 4: Uncropped gels used for Figure 5A-G, 5I-J

368 Figure 5- figure supplement 1- Source Data 1: Raw unedited blots for Figure 5- figure
369 supplement 1C, 1K

370 Figure 5- figure supplement 1- Source Data 2: Uncropped gels used for Figure 5- figure
371 supplement 1C, 1K

Table 1: Yeast 2 Hybrid Interaction Matrix

Interaction Matrix			Selection Medium		
Type	Bait	Prey	DO-2	DO-3	DO-3 + 0.5 mM 3-AT
Positive control	SMAD	SMURF	+	+	/
Negative control	pB66Ø	AD-CYBC1	+	-	-
Negative control	pB66Ø	AD-CYBB	+	-	/
Negative control	DBD-CYBC1	pP7Ø	+	-	/
Negative control	DBD-CYBB	pP7Ø	+	-	-
Interaction	DBD-CYBC1	AD-CYBB	+	-	/
Interaction	DBD-CYBB	AD-CYBC1	+	+	+/-
Interaction	DBD-CYBC1	AD-CYBC1	+	-	/
Interaction	DBD-CYBB	AD-CYBB	+	-	/

Table resuming the different conditions tested during probing of interaction between EROS

(CYBC1) and gp91*phox* (CYBB). pB66: Gal4 DNA-Binding Domain (DBD) vector, i.e. bait vector

(DBD-bait); pB66Ø: empty pB66 vector; pP7: Gal4 Activation Domain (AD) vector, i.e. prey vector (AD-prey). The same AD protein is expressed from both plasmids; pP7Ø: empty pP7 vector; DBD-

CYBC1: aa 1-187 of EROS cloned into pB66. Hybrigenics' reference for this construct is

hgx4414v2_pB66; DBD-CYBB: aa 1-570 of gp91*phox* cloned into pB66. Hybrigenics' reference for

this construct is hgx5346v1_pB66; AD-CYBC1: aa 1-187 of EROS cloned into pP7. Hybrigenics'

reference for this construct is hgx4414v2_pP7; AD-CYBB: aa 1-570 of gp91*phox* cloned into pP7.

Hybrigenics' reference for this construct is hgx5346v1_pP7; DO-2: selective media without

tryptophan and leucine. DO-3: selective media without tryptophan, leucine and histidine. 3-AT: 3-

aminotriazole (see methods).

Key Resources Table				
Reagent type (species) or resource	Designation	Source or reference	Identifiers	Additional information
Genetic reagent (<i>Mus musculus</i>)	C57BL6/N	Jackson Laboratory	RRID:IMSR JAX:005304	Control mice
Genetic reagent (<i>Mus musculus</i>)	Eros/bc017643 ^{tm1a/tm1a}	PMID: 28351984		Eros knockout
Genetic reagent (<i>Mus musculus</i>)	Cybb ^{tm1Din}	Jackson Laboratory	RRID:IMSR JAX:002365	gp91 ^{phox} knockout
Cell line (<i>Mus musculus</i>)	NIH3T3	American Type Culture Collection	CRL-1658	
Cell line (<i>Mus musculus</i>)	RAW 264.7 Eros FLAG-tagged	PMID: 28351984		Macrophages overexpressing tagged Eros
Cell line (<i>Cercopithecus aethiops</i>)	COS-7	American Type Culture Collection	CRL-1651	
Cell line (<i>Homo sapiens</i>)	Control and EROS-deficient human iPS-derived macrophages	This paper		Generated through CRISP-Cas9 technology
Cell line (<i>Homo sapiens</i>)	HEK293, HEK293T,	American Type Culture Collection	CRL-1573 CRL-3216	
Cell line (<i>Homo sapiens</i>)	HEK293-F	Thermo Fisher	R79007	Also known as FreeStyle 293-F Cells
Cell line (<i>Homo sapiens</i>)	HEK293, HEK293 <i>STT3A</i> ^{-/-} , HEK293 <i>STT3B</i> ^{-/-}	PMID: 26864433		Prof Neil Balleid (University of Glasgow)
Cell line (<i>Homo sapiens</i>)	PLB985, EROS-deficient PLB985 (clone 14, clone 20)	DSMZ, PMID: 30312704	ACC 139	Control and EROS knockout lines
Cell line (<i>Homo sapiens</i>)	PLB985 EROS-GFP	PMID: 30312704		Overexpression of EROS

<i>sapiens</i>)				
Antibody	anti-gp91 α (mouse monoclonal) anti-p22 α (rabbit polyclonal) anti-p22 α (mouse monoclonal)	Santa-Cruz Biotechnology	sc-130543 sc-20781 sc-130550	(1:2000) (1:1000) (1:500)
Antibody	anti-C17ORF62/EROS (rabbit polyclonal) anti-P2X7 (rabbit polyclonal)	Atlas Antibodies	HPA045696 HPA044141	(1:1000) (1:500)
Antibody	anti-P2X1 (rabbit polyclonal) anti-P2X4 (rabbit polyclonal) anti-P2X7 (rabbit polyclonal)	Alomone	APR001 APR002 APR004	(1:250) (1:500) (1:500)
Antibody	anti-vinculin (rabbit polyclonal) anti BiP (rabbit polyclonal)	Cell Signalling Technology	4650 C50B12	(1:1000) (1:1000)
Antibody	anti-actin (rabbit polyclonal) anti- α -tubulin (mouse polyclonal)	Abcam	ab8227 ab7291	(1:2000) (1:1000)
Antibody	anti-STT3A (rabbit polyclonal)	Proteintech	12034-1	(1:1000)
Antibody	anti-calnexin (mouse monoclonal)	Invitrogen	MA3-027	(1:1000)
Antibody	anti-FLAG-M2 (mouse monoclonal) anti-FLAG (rat monoclonal)	Sigma Biolegend	F3165 637303	(1:500) (5 μ g)

Antibody	anti-NOX1 (rat monoclonal)	Dr Misaki Matsumoto (Kyoto University, Japan)	31C1	(1:500)
Antibody	anti-NOX4 (rabbit polyclonal)	Prof Ajay Shah (Kings College London, UK)		(1:2000)
Antibody	Mouse anti-CD44-FITC Mouse anti-CD62L-PerCP-Vio700 Mouse anti-CD25-PE-Vio770 Mouse anti-NK1.1-APC Mouse anti-TCR $\gamma\delta$ -Vioblue Mouse anti-CD4-Viogreen	Miltenyi Biotec	clone IM7.8.1 clone REA828 clone 7D4 clone PK136 clone GL3 clone GK1.5	(1:200)
Antibody	Mouse anti-CD8 α -APC Mouse anti-TCR β -BV711	BD Bioscience	clone 53-6.7 clone H57.597	(1:200)
Antibody	Mouse anti-P2X7-PE Mouse anti-CD45-AF700	Biolegend	clone 1F11 clone 30-F11	(1:100)
Recombinant DNA reagent	PCMV6-Kan/Neo <i>Cybb</i>	Origene	MC204867	mouse gp91 $phox$
Recombinant DNA reagent	pCMV6-AC- <i>Cybb</i> -GFP	Origene	MG208975	mouse GFP-tagged gp91 $phox$
Recombinant DNA reagent	pCMV6-Kan/Neo- <i>bc017643</i>	Origene	MC201263	mouse EROS
Recombinant DNA reagent	pCMV6-AC-CYBC1	Origene	SC324452	human EROS
Recombinant DNA reagent	pCMV6-XL4-CYBC1	Origene	SC122091	human gp91 $phox$

Recombinant DNA reagent	pCMV6-AC-CYBB-mRFP	Origene	CW305622	human mRFP-gp91 <i>phox</i>
Recombinant DNA reagent	pCMV6-XL5-CYBA	Origene	SC101113	human p22 <i>phox</i>
Recombinant DNA reagent	pCMV6-AC-NOX4	Origene	SC322623	human NOX4
Recombinant DNA reagent	pCMV6-AC-P2rx7-GFP	Origene	MR227216	mouse GFP-tagged P2X7
Recombinant DNA reagent	pCMV6-XL4-P2RX1	Origene	SC118594	human P2X1
Recombinant DNA reagent	pCMV6-XL5- P2RX4	Origene	SC122124	human P2X4
Recombinant DNA reagent	Human pEGFP-N2-STT3A	PMID: 20693407		Prof. Eric Schirmer, (University of Edinburgh, UK)
Recombinant DNA reagent	human pmRFP-N2-EROS/C17ORF62/CYBC1	PMID: 20693407		Prof. Eric Schirmer, (University of Edinburgh, UK)
Recombinant DNA reagent	human pEGFP-N2-Lap2 β	PMID: 20693407		Prof. Eric Schirmer, (University of Edinburgh, UK)
Recombinant DNA reagent	pEGBacMam-p22 <i>phox</i>	This paper		Human p22 <i>phox</i> construct

Recombinant DNA reagent	pEBacMam-Strep-FLAG-Strep-EROS	This paper		Human EROS construct
Recombinant DNA reagent	pEBacMam-StrepII-FLAG-NOX1	Andrea Mattevi (Dpt. Biology and Biotechnology, University of Pavia, Italy)		Human NOX1 construct
Recombinant DNA reagent	pNGFP-EU-NOX5	This paper		Human NOX5 construct
Peptide, recombinant protein	mouse M-CSF human M-CSF	Peprtech	315-02 300-25	
Peptide, recombinant protein	LPS ATP	Invivogen	LKP-41.02 ATP-41-01	
Commercial assay or kit	Lipofectamine RNAiMAX Lipofectamine 2000	Thermo Fisher	13778075 11668027	
Commercial assay or kit	CD4 L3T4 magnetic beads	Miltenyi Biotech	130-117-043	
Commercial assay or kit	Caspase-Glo 1 inflammasome assay	Promega	G9951	
Commercial assay or kit	Rhod-3-AM calcium imaging kit	Invitrogen	R10145	
Chemical compound, drug	Polyethylenimine	Polyscience Europe GmbH	MW25000	

Chemical compound, drug	PNGase F EndoH	New England Biolabs	P0704S P0702S	
Chemical compound, drug	2,3-O-(4-benzoylbenzoyl) ATP Cycloheximide Tunicamycin Succinylacetone	Sigma Aldrich	5.05734 C4859 SML1287 D1415	
Chemical compound, drug	NGI-1	Tocris	6652	
Software, algorithm	BD FACSDiva v8	BD Biosciences		
Software, algorithm	Velocity 3D Image software	Quorum Technologies Inc.		
Software, algorithm	Fiji is just Image J (version 1.53c) software	PMID: 22930834 PMID: 29187165	RRID: SCR_003070	
Software, algorithm	MASCOT software	Matrix Science		
Software, algorithm	Proteome discoverer, v2.2 and v2.4 software	Thermo Fisher		

Figure 1

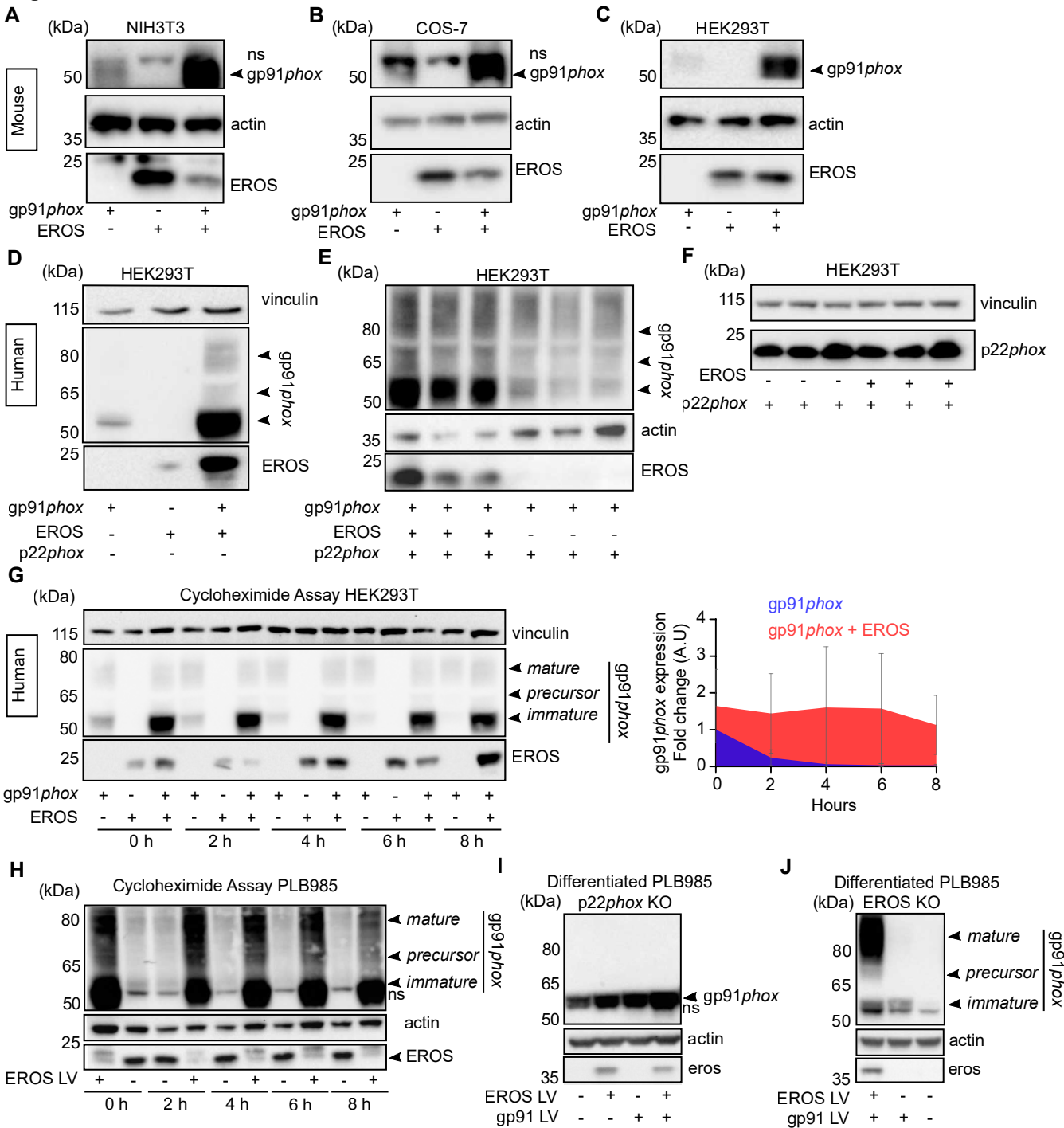
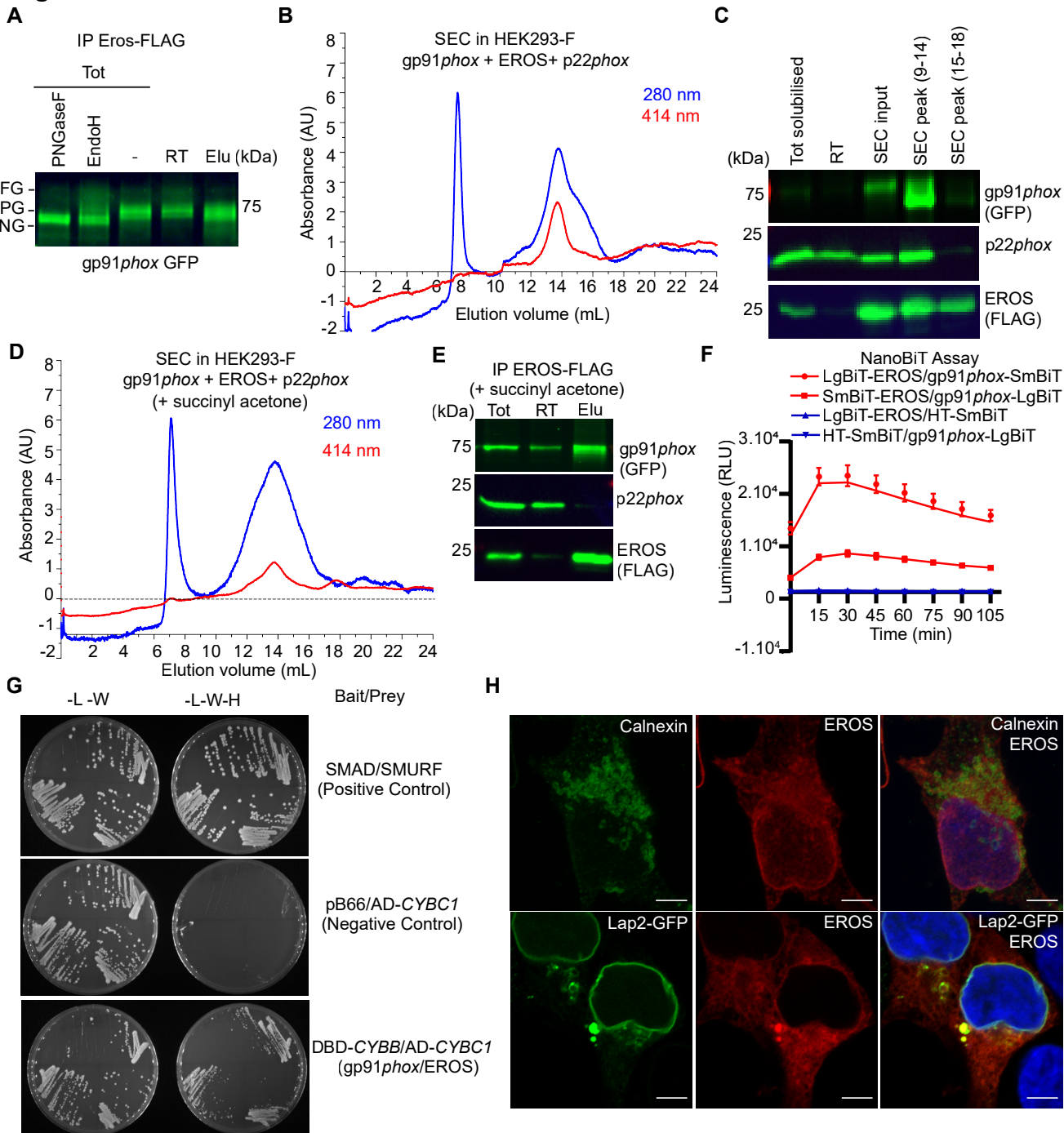


Figure 2

A



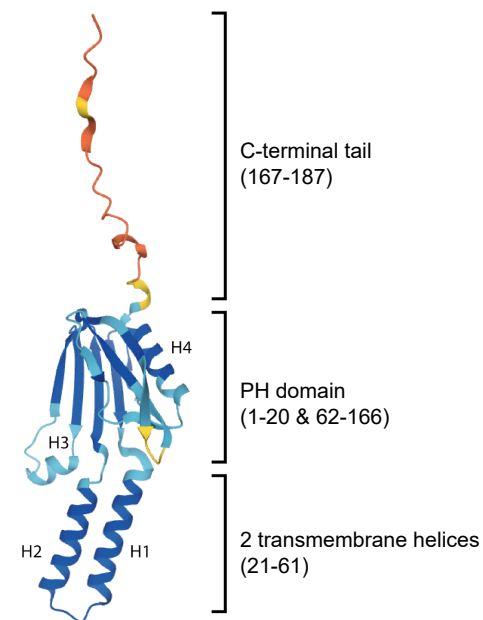
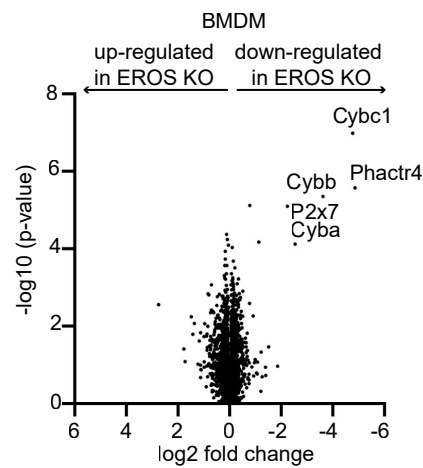
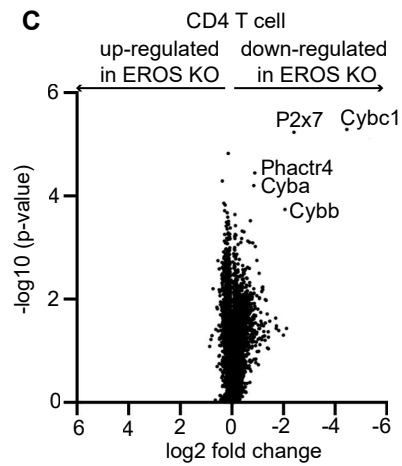
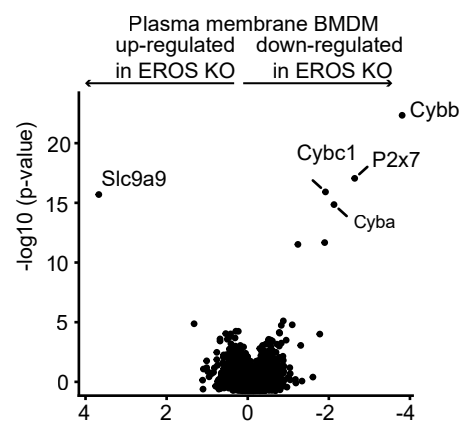
Figure 4**A** EROS Structure Prediction**B****C****D**

Figure 5

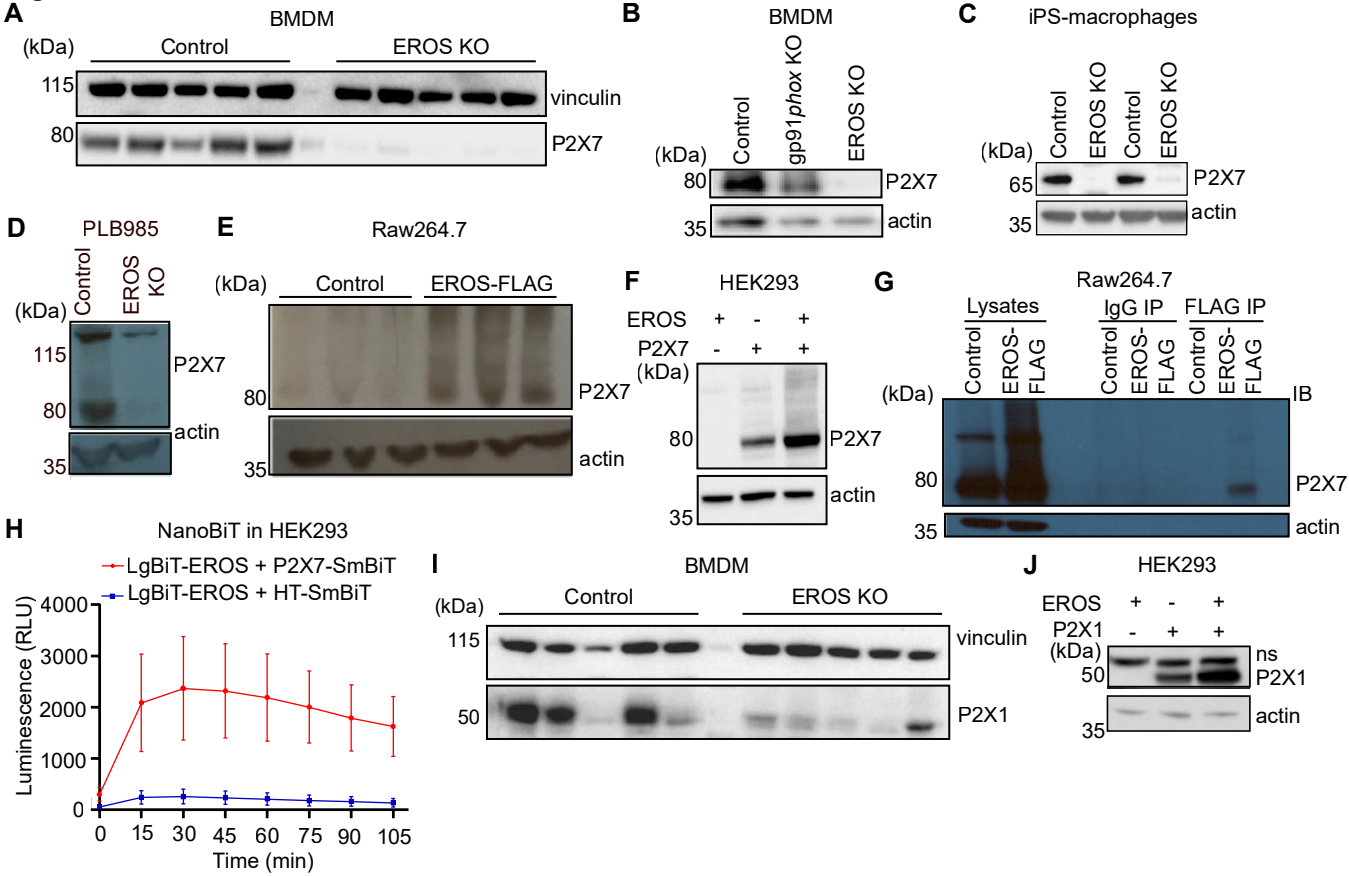


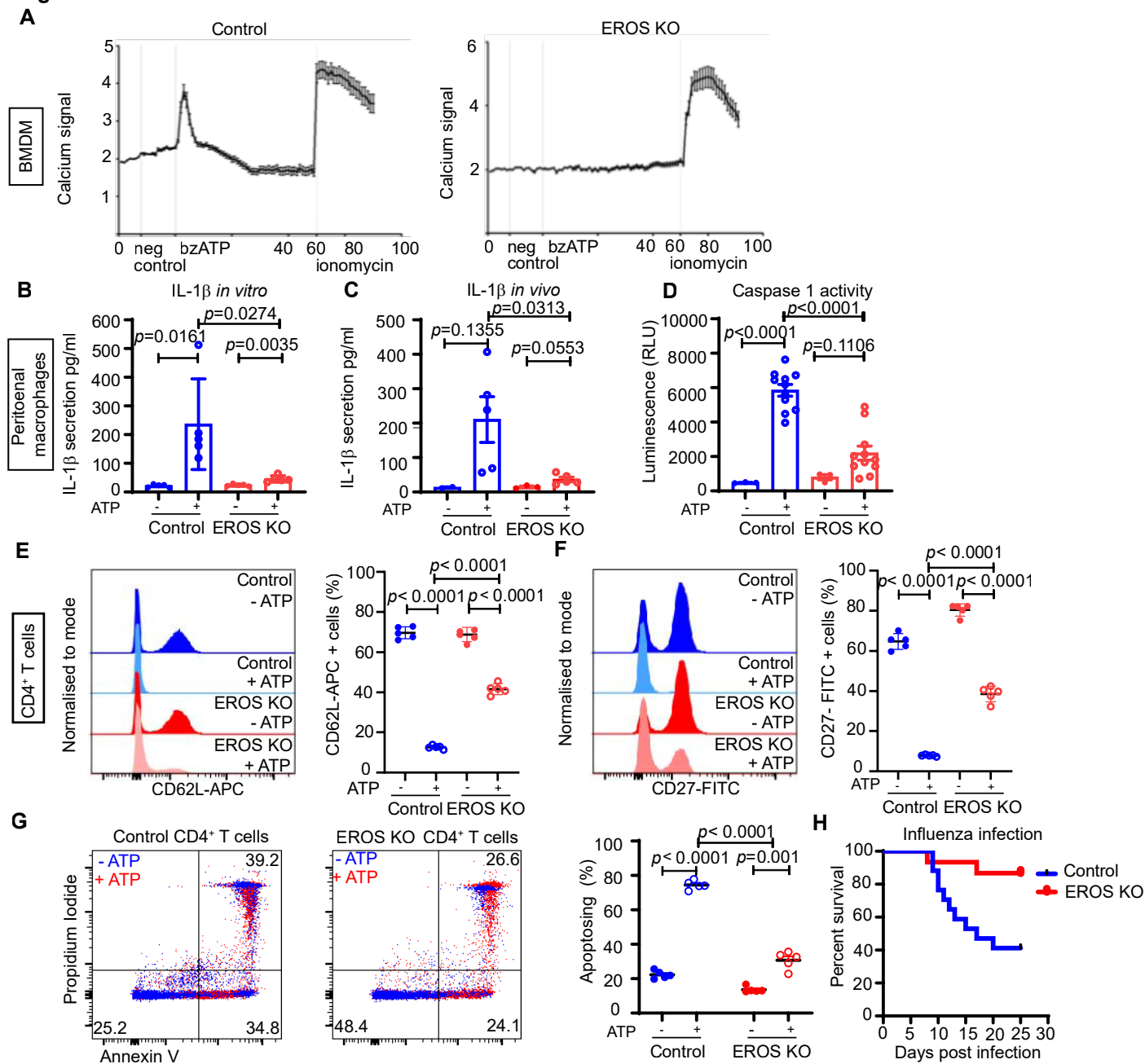
Figure 6

Figure 1 - Figure supplement 1

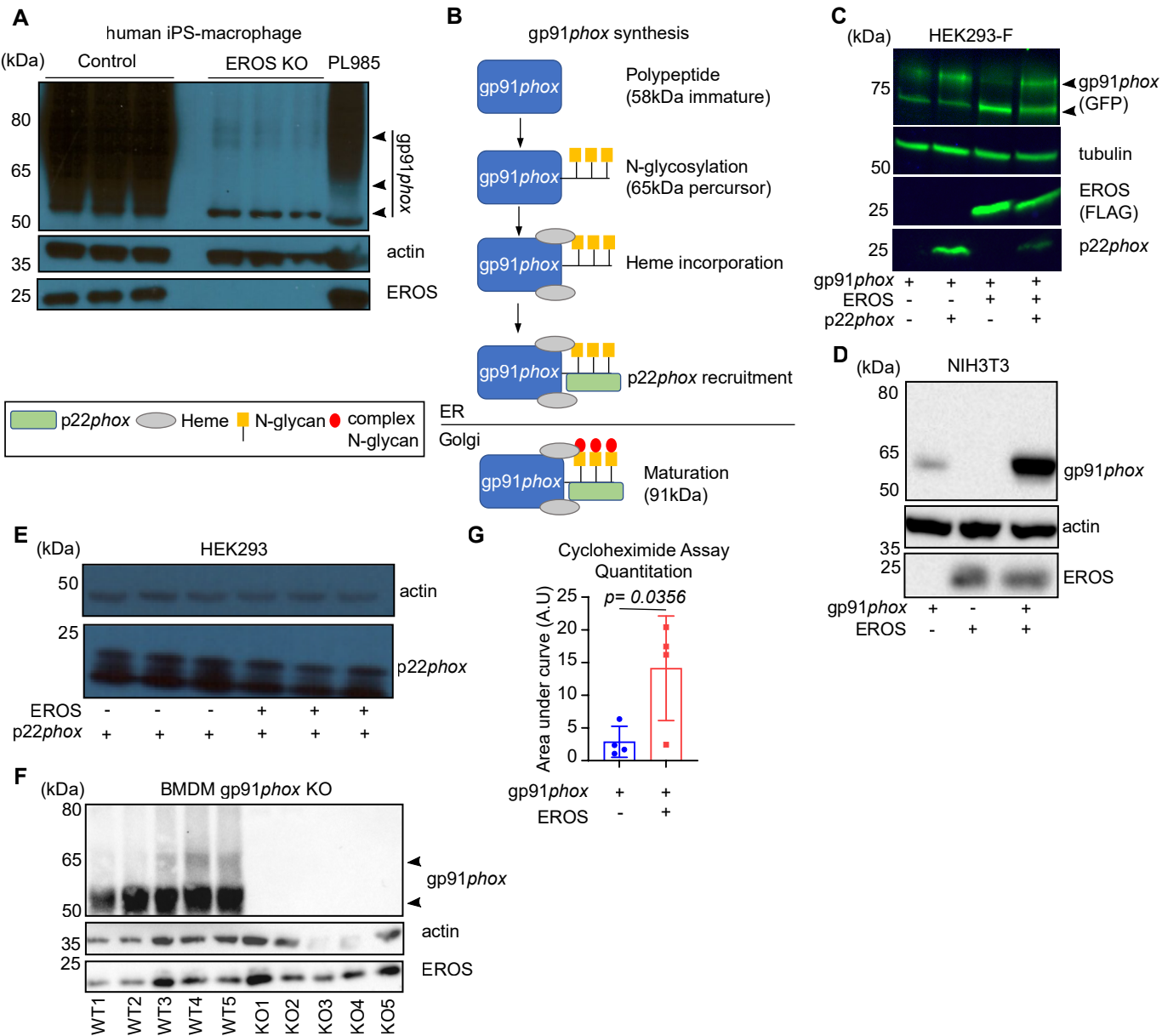


Figure 2 - Figure supplement 1

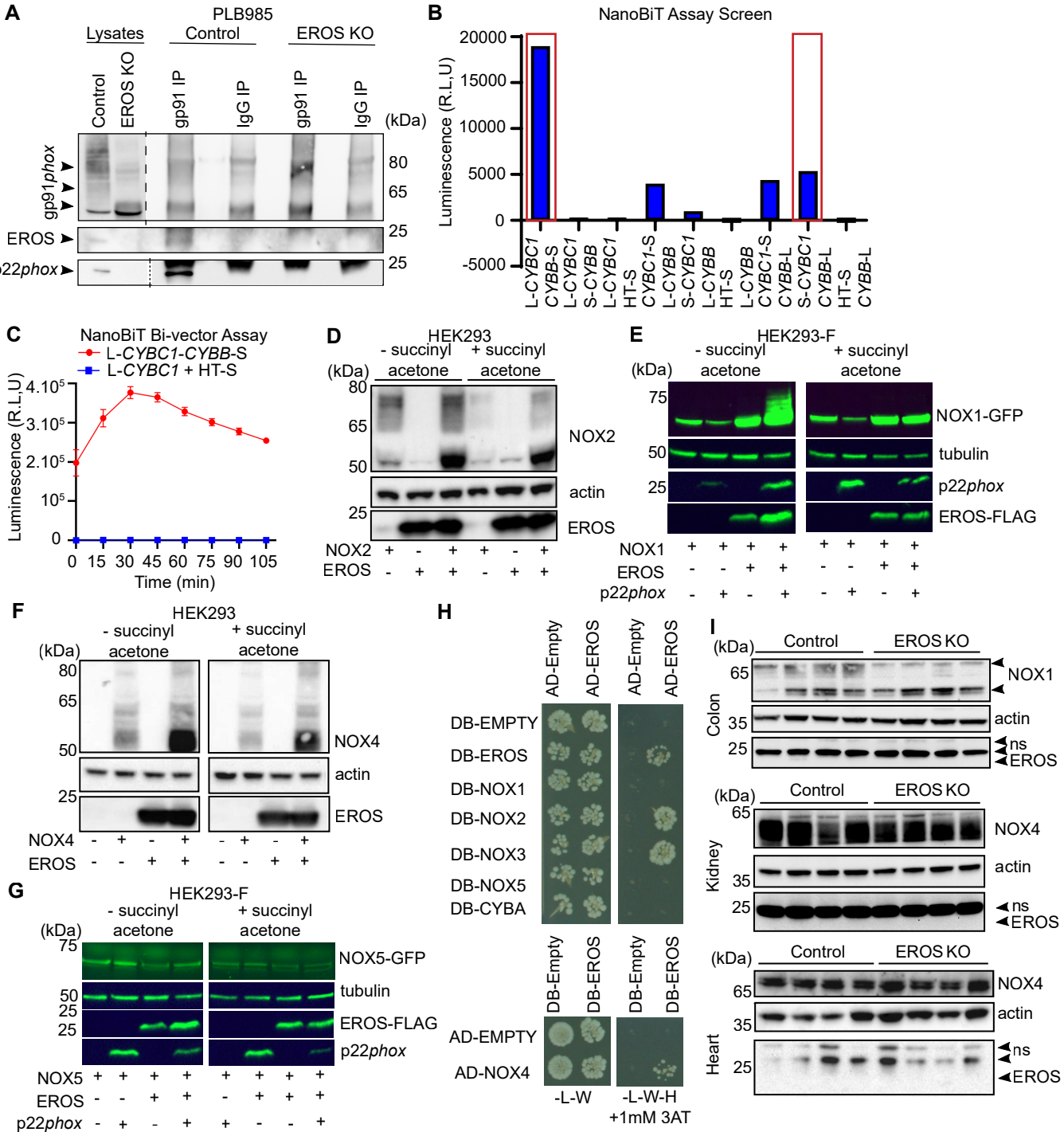


Figure 2 - Figure supplement 2

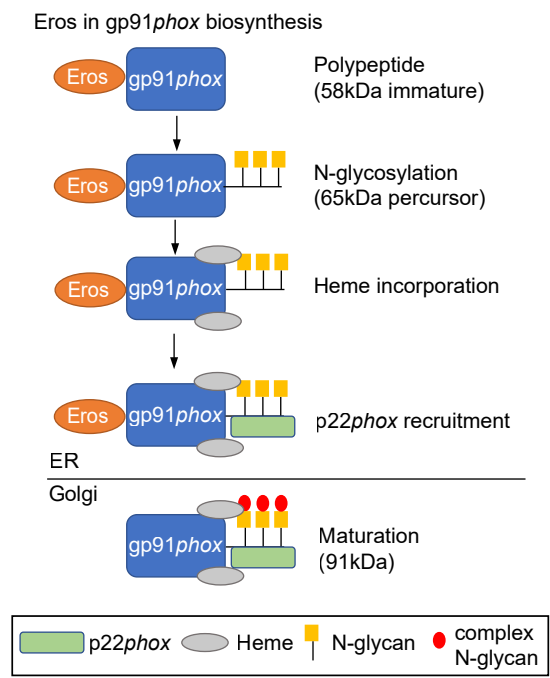
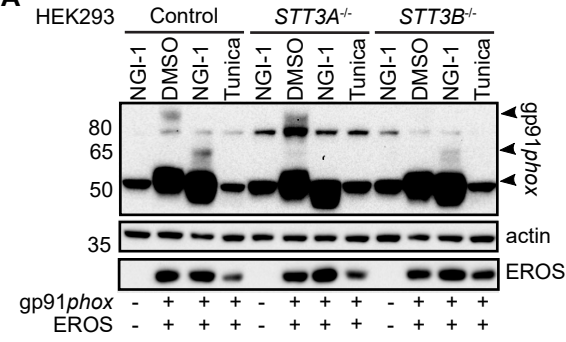
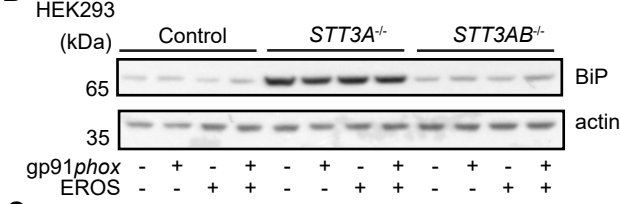


Figure 3 - Figure supplement 1

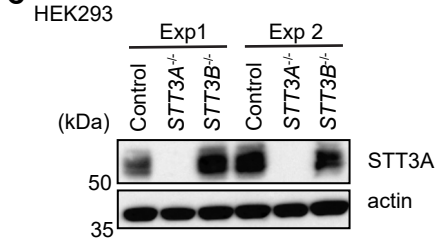
A



B



C



D

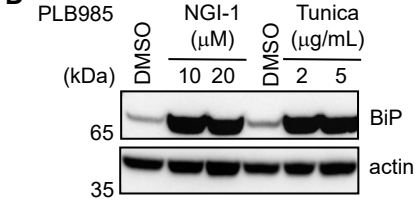


Figure 5 - Figure supplement 1

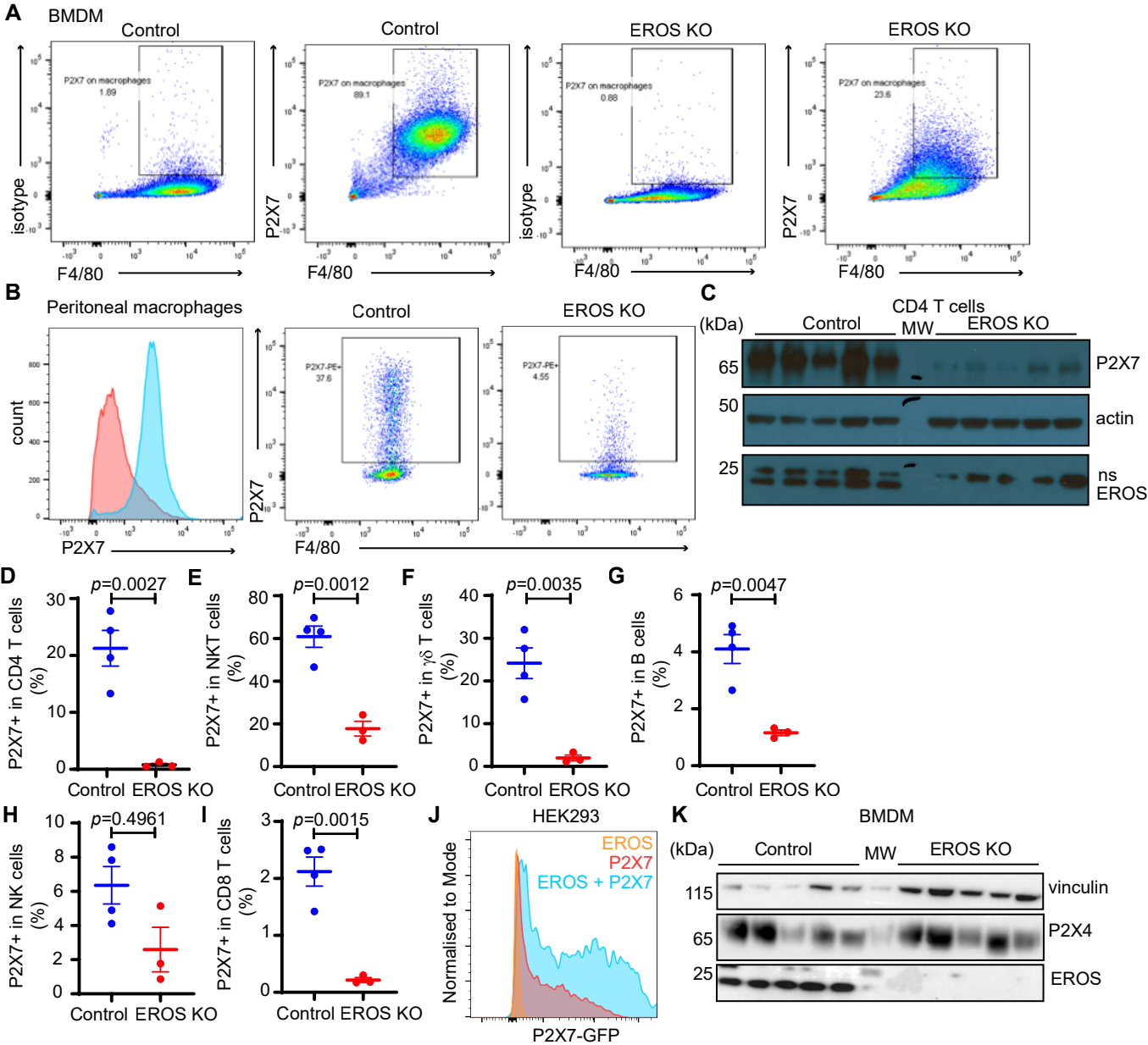


Figure 6 - Figure supplement 1

